

Accretion-powered flares from black hole–disk collisions in galactic nuclei

Joaquin Pelle,^{1*} Kyohei Kawaguchi,^{1,2} Masaru Shibata^{1,2} and Alan Tsz-Lok Lam^{3,4,1}

¹*Max-Planck-Institut für Gravitationsphysik (Albert-Einstein-Institut), Am Mühlenberg 1, D-14476 Potsdam-Golm, Germany*

²*Center of Gravitational Physics and Quantum Information, Yukawa Institute for Theoretical Physics, Kyoto University, Kyoto, 606-8502, Japan*

³*Institute for Gravitation and the Cosmos, The Pennsylvania State University, University Park, PA 16802, USA*

⁴*Department of Physics, The Pennsylvania State University, University Park, PA 16802, USA*

Accepted XXX. Received YYY; in original form ZZZ

ABSTRACT

Black hole impacts on accretion disks in galactic nuclei can power luminous transients, but predicting their observable signatures is challenging because the post-collision flow is highly time-dependent and inhomogeneous. We present a radiative post-processing framework for relativistic hydrodynamics simulations of black hole–disk collisions. Using physically motivated prescriptions for shock heating, optical depth via an eikonal solver, and photon escape fractions that account for advection trapping and diffusion, we predict light curves and spectral energy distributions over a range of disk densities and collision velocities. Our results indicate that the emission is dominated by the long-lived, highly super-Eddington accretion flow onto the secondary black hole, rather than by cooling of the unbound ejecta. In the parameter range explored, the luminosity can reach several times the Eddington luminosity of the secondary, and the emission is generically dominated by soft X-rays. We find that lower velocity collisions produce brighter flares, while the disk surface density mainly controls spectral evolution: low-density disks typically produce \sim keV-peaked flares with weak spectral evolution, whereas high-density disks show softer early emission and late-time hardening. A depletion-time estimate calibrated to our results suggests characteristic durations of hours to days for intermediate-mass secondaries, and yields $t_{\text{flare}} \propto P_{\text{QPE}}$. We discuss implications for QPE-like transients and for the SMBH-binary candidate OJ 287.

Key words: accretion, accretion disks – black hole physics – hydrodynamics – radiative transfer – relativistic processes – X-rays: general

1 INTRODUCTION

Accretion disks around supermassive black holes (SMBHs) are common at galactic centers, particularly during active phases, as in active galactic nuclei (AGNs, Shakura & Sunyaev 1973; Novikov & Thorne 1973; Urry & Padovani 1995; Netzer 2015) or following tidal disruption events (TDEs, Rees 1988; Piran et al. 2015; Mummery & Balbus 2020; Gezari 2021; Dai et al. 2021). At the same time, dense nuclear environments are expected to host a population of compact objects. These may form within the accretion disk through disk fragmentation and subsequent stellar evolution (Goodman & Tan 2004; Levin 2007; McKernan et al. 2012; Stone et al. 2017), or they may be delivered dynamically from the surrounding nuclear star cluster (Bahcall & Wolf 1976, 1977; Alexander 2005; Hopman & Alexander 2006; O’Leary et al. 2009; Antonini & Perets 2012; Antonini 2014; Rose et al. 2022). Interactions between compact objects and accretion disks are therefore a generic outcome of nuclear dynamics and are expected to influence the evolution of the disk and the observational signatures of the nucleus (McKernan et al. 2014; Bartos et al. 2017; Tagawa et al. 2020).

One particularly energetic class of interactions arises when a black hole impacts an accretion disk on a disk-crossing orbit (Ivanov et al.

1998). Due to the typically supersonic velocities involved, such encounters drive strong shocks, and compress and heat the disk gas. The collision triggers a transient accretion flow onto the secondary that can remain in a highly super-Eddington regime for a long time after the collision (Lam et al. 2025). These physical conditions are favorable for the production of very luminous electromagnetic transients.

The discovery of quasi-periodic eruptions (QPEs, Miniutti et al. 2019; Giustini et al. 2020; Arcodia et al. 2021, 2024a; Nicholl et al. 2024; Chakraborty et al. 2021, 2025a; Quintin et al. 2023; Arcodia et al. 2025; Bykov et al. 2025; Hernández-García et al. 2025a; Baldini et al. 2026) has renewed interest in this class of events. QPEs are luminous repeating X-ray flares observed in galactic nuclei hosting SMBHs of $M_c \sim 10^5$ – $10^7 M_\odot$ (Wevers et al. 2022). They exhibit recurrence periods of hours to days, large-amplitude variability, and flare durations typically \sim 10–20% of their recurrence period. The physical origin of QPEs remains uncertain. Several proposed mechanisms involve repeated interactions between orbiting objects and accretion disks (Dai et al. 2010; Xian et al. 2021; Linial & Metzger 2023, 2024; Franchini et al. 2023; Tagawa & Haiman 2023; Linial et al. 2025; Vurm et al. 2025; Yao et al. 2025; Huang et al. 2025; Dodd et al. 2025; Guo & Shen 2026; Suzuguchi & Matsumoto 2026; Jankovič et al. 2026; Huang et al. 2026). Other models include accretion-disk instabilities or oscillations (Sniegowska et al. 2020;

* E-mail: joaquin.pelle@aei.mpg.de

Raj & Nixon 2021; Pan et al. 2022; Kaur et al. 2023; Middleton et al. 2025), recurrent mass transfer from an orbiting companion (Krolik & Linial 2022; Metzger et al. 2022; Zhao et al. 2022; King 2022), and self-lensing in SMBH binaries (Ingram et al. 2021). Black hole–disk collisions are a member of the broader class of orbiter-disk interaction models, and may, in principle, contribute to QPE-like phenomenology.

Black hole–disk impacts have also been invoked in the long-standing interpretation of the blazar OJ 287, whose quasi-periodic optical/UV outbursts motivated binary-SMBH scenarios in which a secondary periodically impacts the primary disk (Sillanpaa et al. 1988; Lehto & Valtonen 1996; Valtonen et al. 2008). Recent analyses have challenged the canonical disk-impact model by the low accretion-disk luminosity inferred from quiescent-state observations (Komossa et al. 2023), while subsequent work has argued that the interpretation did not account for how accretion power is distributed between thermal disk emission and jet production (Valtonen et al. 2023). Regardless of the ultimate nature of OJ 287, predicting the outcomes of black hole–disk collisions can help place constraints relevant to this discussion (e.g., Linial & Metzger 2023; Ressler et al. 2025; Chitan et al. 2026).

Beyond their importance to electromagnetic transients, black hole–disk interactions are also of interest in a multi-messenger context. Compact objects on disk-crossing orbits are expected as extreme-mass-ratio inspiral (EMRI) systems (Amaro-Seoane et al. 2007; Amaro-Seoane 2018), which are key targets for future space-based gravitational-wave observatories like LISA and TianQin (Amaro-Seoane et al. 2017; Babak et al. 2017; Luo et al. 2016). In such environments, disk interactions can influence orbital evolution, modulate accretion onto the central object, and potentially generate electromagnetic counterparts to gravitational waves (Kocsis et al. 2011; McKernan et al. 2012; Bartos et al. 2017; Yang et al. 2019; Sperti et al. 2023; Kejriwal et al. 2024; Duque et al. 2025; Lui et al. 2025; Zhan et al. 2026; Suzuguchi et al. 2026). Even if individual electromagnetic sources are not directly detectable as gravitational-wave sources (e.g. because their characteristic frequencies fall outside the sensitive observational range), constraining the rate and properties of disk interactions can inform the underlying compact-object population, thus aiding the interpretation of the observable EMRI subset (Chen et al. 2022; Zhou et al. 2024a,b; Chakraborty et al. 2025c).

Several studies have investigated aspects of black hole interactions with accretion disks, including analytical estimates (Lehto & Valtonen 1996; Pihajoki 2016; Linial & Metzger 2023; Franchini et al. 2023; Mummery 2025) and (magneto)hydrodynamics simulations of the resulting flows (Ivanov et al. 1998; Suková et al. 2021; Pasham et al. 2024; Ressler et al. 2024, 2025; Lam et al. 2025; Chitan et al. 2026; Liu et al. 2026; Jiang et al. 2026). However, predicting their observable electromagnetic signatures remains challenging. Fully coupled radiation-hydrodynamics simulations (e.g., Ohsuga & Mineshige 2011; Jiang et al. 2014; Sadowski et al. 2017) are computationally expensive and limited in parameter coverage, while purely analytic estimates struggle to capture the complex, time-dependent structure of the post-collision flow. Consequently, predictions for observable light curves and spectral energy distributions (SEDs) remain limited.

We investigate the electromagnetic signatures of black hole–disk collisions by radiative post-processing of relativistic hydrodynamics simulations. Using simulation data from Lam et al. (2025, hereafter, L25), we estimate local energy dissipation due to shock heating, photon escape fractions, and emergent spectra, while accounting for radiative diffusion and advection trapping. This approach allows us

to compute light curves and SEDs over a range of orbital and disk parameters.

Previous models of black hole–disk collisions have generally focused on the emission by cooling of the unbound ejecta produced during the disk impact. Our results, however, suggest that, for a broad region of parameter space, the dominant source of radiation is instead the highly super-Eddington accretion flow (e.g., Inayoshi et al. 2016; Kitaki et al. 2018, 2021; Toyouchi et al. 2024) that develops around the secondary black hole after the collision, producing long-lived soft X-ray flares.

This paper is organized as follows. In Sec. 2 we describe the physical setup and characteristic scales of the black hole–disk collision scenario. Sec. 3 summarizes the radiative post-processing framework, including shock heating, optical depth calculations, and emergent SEDs. Sec. 4 presents the resulting bolometric- and specific-luminosity light curves along with time-averaged SEDs. In Sec. 5, we discuss astrophysical implications of our results. We conclude in Sec. 6 with a summary and a discussion of limitations and prospects for future work. Throughout this paper, G , c , and k_B denote the gravitational constant, speed of light, and Boltzmann’s constant, respectively.

2 PHYSICAL SETUP

We consider the interaction between an orbiting black hole of mass m_{BH} (hereafter, the secondary) and the accretion disk surrounding a supermassive black hole (SMBH) of mass M_c (the primary). The secondary crosses the disk with a relative velocity v , which we take to be the local Keplerian orbital velocity at the crossing radius. The disk is characterized locally by its surface density Σ , vertical scale height H , central sound speed $c_{s,\text{max}}$ and polytropic index Γ . Throughout this work, these quantities are understood as local disk properties evaluated at the orbital radius of the secondary. A characteristic timescale is the disk-crossing time $t_{\text{cross}} := 2H/v$. For convenience, we also define the dimensionless scale height, $h := H/r_g$, where $r_g := Gm_{\text{BH}}/c^2$ is the gravitational radius of the secondary.

A useful interaction length scale is the accretion radius of the secondary,

$$r_a := \frac{2Gm_{\text{BH}}}{v^2} \approx 1.1 \times 10^{12} m_{\text{BH},4} v_{0.05}^{-2} \text{ cm}, \quad (1)$$

which sets the characteristic size of the region from which disk material is gravitationally focused toward the secondary during the encounter. Here, $m_{\text{BH},4} := m_{\text{BH}}/(10^4 M_\odot)$, and $v_{0.05} := v/(0.05c)$. Associated with this scale is the characteristic intercepted mass,

$$m_a := \pi r_a^2 \Sigma \approx 4.4 \times 10^{28} m_{\text{BH},4}^2 v_{0.05}^{-4} \Sigma_4 \text{ g}, \quad (2)$$

and the corresponding mass flux,

$$\dot{m}_a := \pi r_a v \Sigma \approx 5.6 \times 10^{25} m_{\text{BH},4} v_{0.05}^{-1} \Sigma_4 \text{ g/s}, \quad (3)$$

where $\Sigma_4 := \Sigma/(10^4 \text{ g cm}^{-2})$. For comparison, we define the Eddington accretion rate of the secondary as $\dot{m}_{\text{Edd,BH}} := 10 L_{\text{Edd,BH}}/c^2$, where $L_{\text{Edd,BH}} = 4\pi Gcm_{\text{BH}}/\kappa \approx 1.4 \times 10^{42} m_{\text{BH},4} \text{ erg s}^{-1}$ is the Eddington luminosity of the secondary and we assumed a radiative efficiency of 10% and opacity $\kappa \approx 0.34 \text{ cm}^2 \text{ g}^{-1}$. In terms of this rate, we can write

$$\dot{m}_a \approx 3.7 \times 10^3 v_{0.05}^{-1} \Sigma_4 \dot{m}_{\text{Edd,BH}}. \quad (4)$$

Therefore, typical accretion rates can be highly super-Eddington. These scalings also suggest that the collision outcome is highly sensitive to the impact velocity. Because $r_a \propto v^{-2}$, the intercepted mass

Table 1. Main symbols used in this work.

Symbol	Meaning
M_c	Mass of the central SMBH (primary)
m_{BH}	Mass of the impactor BH (secondary)
r_g	Gravitational radius of the secondary, Gm_{BH}/c^2
t_g	Gravitational time of the secondary, Gm_{BH}/c^3
v	Relative velocity of the secondary through the disk
Σ	Disk surface density at the crossing radius
H	Disk scale height at the crossing radius
h	Dimensionless disk scale height, H/r_g
r_a	Accretion radius, $2Gm_{\text{BH}}/v^2$
m_a	Characteristic intercepted mass, $\pi r_a^2 \Sigma$
\dot{m}_a	Characteristic mass flux, $\pi r_a v \Sigma$
t_{cross}	Disk crossing time, $2H/v$
$L_{\text{Edd,BH}}$	Eddington luminosity of the secondary black hole
R	Orbital radius of the secondary around the primary
P_{orb}	Orbital period of the secondary around the primary
P_{QPE}	Fiducial QPE recurrence period, $P_{\text{orb}}/2$

depends steeply on velocity, $m_a \propto v^{-4}$. Thus, slower encounters intercept substantially more gas and supply a larger energy reservoir to feed the post-collision accretion flow, whereas faster encounters are naturally less energetic even if they remain super-Eddington (because $\dot{m}_a \propto v^{-1}$). As we show in Sec. 4, our results confirm these expectations.

For the fluid variables, we use data from the relativistic hydrodynamics simulations in L25, which were performed with the SACRA-2D code (Lam & Shibata 2025). In those simulations, the Euler equations are solved in the frame of the secondary, and the disk is initially assumed to move with uniform vertical velocity towards the secondary in that frame. Prior to the encounter, the disk is modeled locally as a horizontally homogeneous fluid slab in vertical hydrostatic equilibrium under the gravity of the primary (which is not in the simulation domain). The fluid is assumed to follow a Γ -law equation of state with $\Gamma = 4/3$, corresponding to the radiation-pressure dominated regime. The vertical gravitational field due to the primary is approximated as linear in height above the midplane, with a phenomenological cutoff at a height z_{cut} . For more details on the simulation setup, we refer the reader to L25.

Several assumptions underlie our post-processing approach. First, we neglect radiative feedback on the gas dynamics. This should be regarded as a limitation of the present framework, since radiation forces and cooling could modify the structure of the post-collision flow. Quantifying the accuracy of this approximation will require radiation-hydrodynamics simulations, which are beyond the scope of the present work. Second, even though the simulations are performed in general relativity (GR), we do not include GR corrections in the radiative calculations. This simplification is expected to be adequate because the regions that dominate the observable emission are typically located at distances from the secondary where GR effects are subdominant. The innermost regions close to the event horizon, where strong-field effects are important, are largely hidden from view by the high optical depth.

3 RADIATIVE POST-PROCESSING FRAMEWORK

We map hydrodynamic snapshot data to estimates of electromagnetic observables by volume integrals of the form:

$$L_{\text{bol}}(t) \approx \int \dot{\epsilon}(\mathbf{x}, t) f_{\text{esc}}(\mathbf{x}, t) dV, \quad (5)$$

where L_{bol} is the bolometric luminosity, $\dot{\epsilon}$ is the local photon energy generation rate density and f_{esc} is an effective escape fraction capturing advection trapping and finite diffusion time effects. For the specific luminosities, we add a local spectral-weighting factor to the integrand in a manner we detail further below.

3.1 Local energy generation rate density $\dot{\epsilon}$

We compute $\dot{\epsilon}$ based on a shock-heating estimator. For a planar shock of area A and shock speed v_{sh} , the energy generation rate across the shock is written as

$$\dot{E} = A \rho_u (v_u - v_{\text{sh}}) (\epsilon_d - \epsilon_u), \quad (6)$$

where ρ , ϵ , and v are the density, specific internal energy, and velocity in the frame of the secondary, respectively, and subscripts u and d denote upstream and downstream states. In discrete form, across a cell interface of area ΔA , assigned to a downstream cell volume ΔV , we define

$$\dot{\epsilon} \Delta V = \Delta A \rho_u (v_u - v_{\text{sh}}) (\epsilon_d - \epsilon_u). \quad (7)$$

We refer the reader to Appendix A for details on the shock identification criteria and shock speed calculation.

3.2 Optical depth

The photon escape fraction is tied to the optical depth in the medium. In a scattering-dominated, optically thick medium, photons preferentially escape along paths of least integrated optical depth. To model photon escape in such a medium, we compute the optical depth field $\tau(\mathbf{x})$ as a minimum over paths between \mathbf{x} and the boundary of the domain $\partial\Omega$,

$$\tau(\mathbf{x}) = \min_{\gamma \in C(\mathbf{x})} \int_{\gamma} \kappa \rho dl, \quad (8)$$

where $C(\mathbf{x})$ is the set of smooth paths starting from any point in $\partial\Omega$ and ending in \mathbf{x} . This choice is motivated by the fact that, in strongly inhomogeneous and anisotropic flows such as those following a black hole–disk collision, the minimum-escape paths are generically not along a fixed geometric direction (e.g., radial or vertical as often assumed). Therefore, an optical depth defined along, for example, radial rays, would not be adequate to capture the true escape fraction, as it may artificially block regions of the gas in a highly non-spherical geometry. This approach is inspired by that used in some neutrino-leakage schemes (e.g., Perego et al. 2014).

The global optimization problem as formulated in Eq. (8) is not suitable for direct solution. Instead, we rely on the property that the desired solution satisfies an eikonal equation,

$$|\nabla\tau| = \kappa\rho, \quad \tau|_{\partial\Omega} = 0, \quad (9)$$

which we solve using a fast-sweeping method (Zhao 2005) implemented in the Julia package Eikonal.jl, with modifications to enable the multi-block grids on which our hydrodynamic data is given. From each cell, we recover minimum-escape paths γ_{esc} and path lengths $\ell_{\text{esc}}(\mathbf{x})$ by gradient descent along $-\nabla\tau$.

We adopt a constant opacity $\kappa = 0.34 \text{ cm}^2 \text{ g}^{-1}$ for the optical-depth computation, consistent with electron scattering in a fully ionized gas with cosmic composition, the dominant opacity in the temperature and density range relevant for the post-collision flow. True absorption processes (mainly free–free) are subdominant for the total optical depth but remain important for photon production and thermalization. These effects intervene in the photon temperature estimate described in Sec. 4.3. We have verified that true absorption does not

significantly attenuate the escaping radiation, and therefore use only the electron-scattering opacity for the escape fraction (see Sec. 4.3 for more details).

3.3 Escape fraction

In the optically thick regime, photon escape is regulated by diffusion and advection of radiation with the flow. We model these effects by implementing the escape fraction as a product of two factors,

$$f_{\text{esc}}(\mathbf{x}, t) := f_{\text{adv}}(\mathbf{x}, t) f_{\text{diff}}(\mathbf{x}, t), \quad (10)$$

representing suppression by advection trapping and by finite diffusion time, respectively.

3.3.1 Advection trapping

Our advection-trapping factor is motivated by a steady toy model constructed on top of an underlying hydrodynamic profile (see Appendix B for the details). The factor is locally defined along the corresponding minimum-escape path γ_{esc} as:

$$f_{\text{adv}} := \exp\left[-\frac{4}{c} \int_{\gamma_{\text{esc}}} v^- d\tau\right], \quad v^- := \min(v_r, 0), \quad (11)$$

where v_r is the radial velocity component and $d\tau = \kappa\rho d\ell$ is the differential optical depth along γ_{esc} . This prescription attenuates radiation generated in regions where large optical depth and inward advection would tend to drive photons inward, thereby suppressing photon escape.

3.3.2 Finite diffusion-time suppression

We estimate the diffusion time as

$$t_{\text{diff}}(\mathbf{x}, t) := \tau(\mathbf{x}, t) \ell_{\text{esc}}(\mathbf{x}, t)/c, \quad (12)$$

and apply an attenuation relative to the time elapsed from a reference collision time $t_{\text{coll}} = t_{\text{cross}} := 2H/v$,

$$f_{\text{diff}} := \exp\left[-\frac{t_{\text{diff}}}{t - t_{\text{coll}}}\right]. \quad (13)$$

Equations (11)–(13) define the escape fraction used in (5).

3.4 Local photon temperature

To predict the emerging specific luminosities at given frequencies, we need to estimate the spectral distribution of photons emitted from each region of the flow. For this purpose, we first define an estimated local photon temperature following arguments from Nakar & Sari (2010), as we detail in the rest of this section.

We take the local energy budget and average photon energy as

$$e \approx \rho\varepsilon, \quad \langle\varepsilon_\gamma\rangle := \frac{e}{n_\gamma}, \quad (14)$$

where n_γ is the photon number density. In optically thick regions, with strong electron–photon coupling, free–free emission produces photons until the typical photon energy $3k_B T$ approaches the typical electron energy. In terms of the free–free photon production rate, the number density reads $n_\gamma \approx t_{\text{diff}} \dot{n}_{\text{ff}}(\rho, T) \xi(T)$, where $\dot{n}_{\text{ff}} \approx 3 \times 10^{36} \text{ cm}^{-3} \text{ s}^{-1} \rho^2 T^{-1/2}$ is the production rate of photons at energy $3k_B T$, and $\xi(T)$ is a logarithmic correction factor accounting for free–free photons that are produced at lower energies that can be Comptonized to energy $3k_B T$ (see Nakar & Sari (2010) for its

definition), and we take the diffusion time t_{diff} as an estimate of the escape time of the photons¹. Combining this with Eq. (14) gives an implicit equation for the temperature estimate:

$$\frac{\rho\varepsilon}{3k_B T} = t_{\text{diff}} \dot{n}_{\text{ff}}(\rho, T) \xi(T). \quad (15)$$

We denote the local solution to this equation as T_{ff} .

We further constrain the temperature thus obtained by imposing upper and lower bounds. First, the temperature cannot fall below the blackbody temperature corresponding to the local radiation energy density, $T_{\text{BB}} := (\rho\varepsilon/a_{\text{rad}})^{1/4}$, with a_{rad} the radiation constant, since photons of lower energy would be absorbed rather than emitted. Additionally, we impose an upper bound associated with pair production from photon–photon absorption. At sufficiently high temperatures, photon–photon interactions efficiently produce electron–positron pairs, increasing the lepton number density and degrading the photon energy. This regulates the radiation temperature to remain below $T_{\gamma\gamma} \sim 100\text{--}200 \text{ keV}$ (Weaver 1976; Katz et al. 2010). Therefore, we cap the inferred temperature at $T_{\gamma\gamma}$ to account for this self-regulation in a phenomenological manner. Finally, we require that the photon temperature does not exceed the virial temperature associated with the local specific internal energy, $T_{\text{vir}} := (\Gamma - 1)\mu m_p \varepsilon/k_B$ with μ the mean molecular weight per particle and m_p the proton mass, corresponding to a situation where the internal energy resides entirely in the motion of the gas particles. In summary, the temperature assigned to each cell is defined as $T = \min(\max(T_{\text{BB}}, T_{\text{ff}}), T_{\gamma\gamma}, T_{\text{vir}})$.

This scheme implicitly assumes that the bulk of internal energy is carried by radiation rather than by electrons. A posteriori, we can check the consistency of this assumption by estimating the electron internal energy density, $e_e \approx 3n_e k_B T$, where the electron number density is inferred from the mass density as $n_e = \rho/(\mu_e m_p)$ with μ_e the mean molecular weight per electron. For the photon-dominated assumption to be self-consistent, the electron energy density must satisfy $e_e \ll \rho\varepsilon$. If this condition were violated, electrons would carry a significant fraction of the internal energy and could not be assumed to efficiently transfer their energy to photons on the diffusion timescale, invalidating the energy budget underlying Eq. (15). In that case, more careful consideration of the electron advection and cooling timescales would be required. However, we have checked that regions where this consistency condition is not satisfied contribute negligibly to the escaping radiation. We therefore neglect the contribution to the light curves and spectra from such a region.

Another underlying assumption of this scheme is strong electron–photon coupling, which requires large scattering optical depth and diffusion timescales. In optically thin regions ($\tau \lesssim 1$), photons escape before equilibrating with the electrons, and the typical photon energy would instead be set by the instantaneous electron temperature and the free–free emissivity, requiring a different treatment. In practice, however, we find that the dominant contribution to the observed radiation originates in regions with $\tau > 1$, where the assumptions leading to Eq. (15) are reasonably satisfied. We therefore neglect optically thin regions in the temperature post-processing without significant loss of accuracy for the parameter range considered here.

Finally, we have verified that considering free–free absorption in the optical depth does not affect the results. Defining a free–free absorption opacity as $\kappa_{\text{abs}} \sim \dot{n}_{\text{ff}}(\rho, T_{\text{BB}})/(c\rho n_{\text{BB}}(T_{\text{BB}}))$, where $n_{\text{BB}}(T_{\text{BB}})$ is the blackbody photon number density at T_{BB} , one may

¹ Strictly speaking, one could replace t_{diff} by $\min(t - t_{\text{coll}}, t_{\text{diff}})$. We have verified that this modification does not affect the results, so we keep the simpler expression.

estimate an absorption optical depth $\tau_{\text{abs}} \sim \kappa_{\text{abs}} \rho \ell_{\text{esc}}$. The corresponding effective absorption optical depth is then $\tau_{\text{eff}} \sim \sqrt{\tau_{\text{abs}} \tau}$, where τ is the scattering optical depth defined in Section 3.2. In the scattering-dominated regime relevant here, we find $\tau_{\text{eff}} \ll \tau$, and including an attenuation factor $\exp(-\tau_{\text{eff}})$ does not produce significant changes in the light curves. This supports our use of scattering optical depth alone in the escape fraction.

3.5 Specific luminosities

Once the local temperature map throughout the flow has been obtained, we define rough estimates of the specific luminosity at a given frequency ν in volume-integral form as

$$\nu L_{\nu} \approx \nu \int \dot{e} f_{\text{esc}} \frac{\pi B_{\nu}(T)}{\sigma T^4} dV, \quad (16)$$

where $\sigma = a_{\text{rad}} c/4$ is the Stefan-Boltzmann constant, B_{ν} is the Planck function, and the integral is restricted to the optically thick, photon-dominated region where the assumptions underlying our temperature calculation are satisfied. Note that the weighting factor implicitly assumes that photons are thermally distributed at temperature T , which is not necessarily true. This spectral weighting should therefore be interpreted as a diagnostic of characteristic photon energies rather than a detailed prediction of an exact spectral shape. Alternatively, we could use a spectral weight proportional to the free-free emissivity. We have verified that this produces a modest broadening of the SED, particularly enhancing emission at lower photon energies (e.g., ~ 100 eV) relative to the ~ 1 keV peak. This does not affect the qualitative trends and our main conclusions, and we therefore retain the blackbody weighting in Eq. (16) for simplicity.

3.6 Limitations of the present framework

Several limitations should be kept in mind when interpreting our results. First, the hydrodynamics simulations neglect radiation forces and radiative cooling, which could modify the gas dynamics, in both optically thick and optically thin regions. Radiation-hydrodynamics simulations will be required to quantify these effects more precisely in the future. Second, our radiative post-processing framework approximates photon escape using a minimum-escape optical-depth prescription and therefore does not capture the angular dependence of the emergent radiation field. Third, the simulations are local, i.e., we focus on the local interaction between the secondary black hole and the accretion disk around the primary, and do not include the global structure of the disk or the orbital evolution of the secondary.

Despite these simplifications, the main conclusions of this work rely primarily on robust hydrodynamic features of the collision, namely the formation of a shocked wake and the development of a long-lived super-Eddington accretion flow. These features would plausibly persist in more realistic radiation-hydrodynamics simulations, although their detailed radiative properties may change.

4 RESULTS

4.1 Parameter space

The simulations analyzed here are drawn from the suite presented in L25. Since fluid self-gravity is neglected, the hydrodynamic evolution is invariant under a rescaling of the gas density. As a result, the simulations are characterized primarily by the collision velocity ν and the dimensionless disk thickness H/r_g .

Although the original simulation suite spans a broader range of velocities, in this work we focus on a representative subset of models with collision velocities $\nu = 0.05c$, $0.1c$, and $0.2c$, which samples different velocity regimes. The simulations also include several values of the disk scale height, $H = 200$, 500 , and $1000 r_g$. Within this range the qualitative properties of the post-collision flow depend only weakly on H/r_g compared to their dependence on ν , so for clarity the analysis presented below focuses on the $H = 1000 r_g$ models. We show below that the relevant emission timescales are much longer than the disk-crossing time, so H is expected to impact at most the earliest stages of the evolution.

The radiative post-processing introduces a physical mass scale via the optical depth $\tau \sim \kappa \rho \ell$. We therefore assign physical values to the disk surface density when computing radiative diagnostics on top of the simulation data. In this work we consider $\Sigma = 10^3$, 10^4 , 10^5 , and 10^6 g cm $^{-2}$, which span a broad range expected for accretion disks in galactic nuclei at radii relevant for nuclear transients.

The secondary mass m_{BH} mainly sets the physical normalization of the problem. At fixed collision velocity ν and dimensionless disk thickness H/r_g , one has $\rho \propto \Sigma/m_{\text{BH}}$, $\dot{e} \propto \Sigma/m_{\text{BH}}^2$, and $\tau \sim \kappa \rho \ell_{\text{esc}} \propto \Sigma$. Consequently, the bolometric luminosity in Eddington units, $L_{\text{bol}}/L_{\text{Edd,BH}}$, is independent of m_{BH} for fixed (ν, Σ) . The role of m_{BH} is therefore mainly to set the physical luminosity and timescale normalizations, with only an additional effect on the spectrum through the local temperature estimate. As we show in Sec. 4.3.1, this spectral dependence is weak within the intermediate-mass black hole (IMBH) range.

4.2 Bolometric emission

In this section, we analyze the bolometric luminosity generated by the interaction between the black hole and the disk. Qualitatively, the evolution of the flow and radiative output can be split into two broad phases: when the black hole emerges from the disk, a reverse Bondi–Hoyle–Lyttleton (Hoyle & Lyttleton 1939; Bondi & Hoyle 1944; Edgar 2004) shock forms and dominates the emission. As the flow evolves, the BHL-shock contribution dims, a convective region becomes active, and the luminosity becomes dominated by this region. We illustrate this in Fig. 1 where we show the rest-mass density and the local contributions to the total bolometric luminosity ($\dot{e} f_{\text{esc}}$) at different times during the evolution, together with a set of optical-depth contours, for a representative case $\Sigma = 10^4$ g cm $^{-2}$ and $\nu = 0.05c$, with normalizations corresponding to $m_{\text{BH}} = 10^4 M_{\odot}$. Considering $2\pi R \dot{e} f_{\text{esc}}$ instead, i.e., weighting the emission by the cylindrical volume element, does not qualitatively change the picture. The dominant emission still comes from the same shocked structures, with only a modest reweighting toward larger cylindrical radii.

Fig. 2 shows the bolometric light curves. The accretion-powered emission typically persists for a substantial fraction of the simulated interval, of order ~ 10 – $30 t_{\text{cross}}$ depending on the model. For reference, the disk-crossing time scales as $t_{\text{cross}} = 4 \times 10^4 t_g \nu_{0.05}^{-1} h_3$, where $h_3 := h/10^3$ and $t_g := Gm_{\text{BH}}/c^3$. Thus, for the models shown in Fig. 2, a duration of ~ 10 – $30 t_{\text{cross}}$ corresponds to $\sim 10^5$ – $10^6 t_g$, and the same extent in t/t_{cross} corresponds to a longer physical duration for lower collision velocities.

Across most of the explored parameter space, the bolometric luminosity reaches values of order 0.1 – $10 L_{\text{Edd,BH}}$. The most luminous models, corresponding to relatively low velocities and low/intermediate surface densities, sustain luminosities of several $L_{\text{Edd,BH}}$. In contrast, the faintest models, mainly at $\nu = 0.2c$, remain $\lesssim 0.1 L_{\text{Edd,BH}}$ because the intercepted gas mass decreases steeply

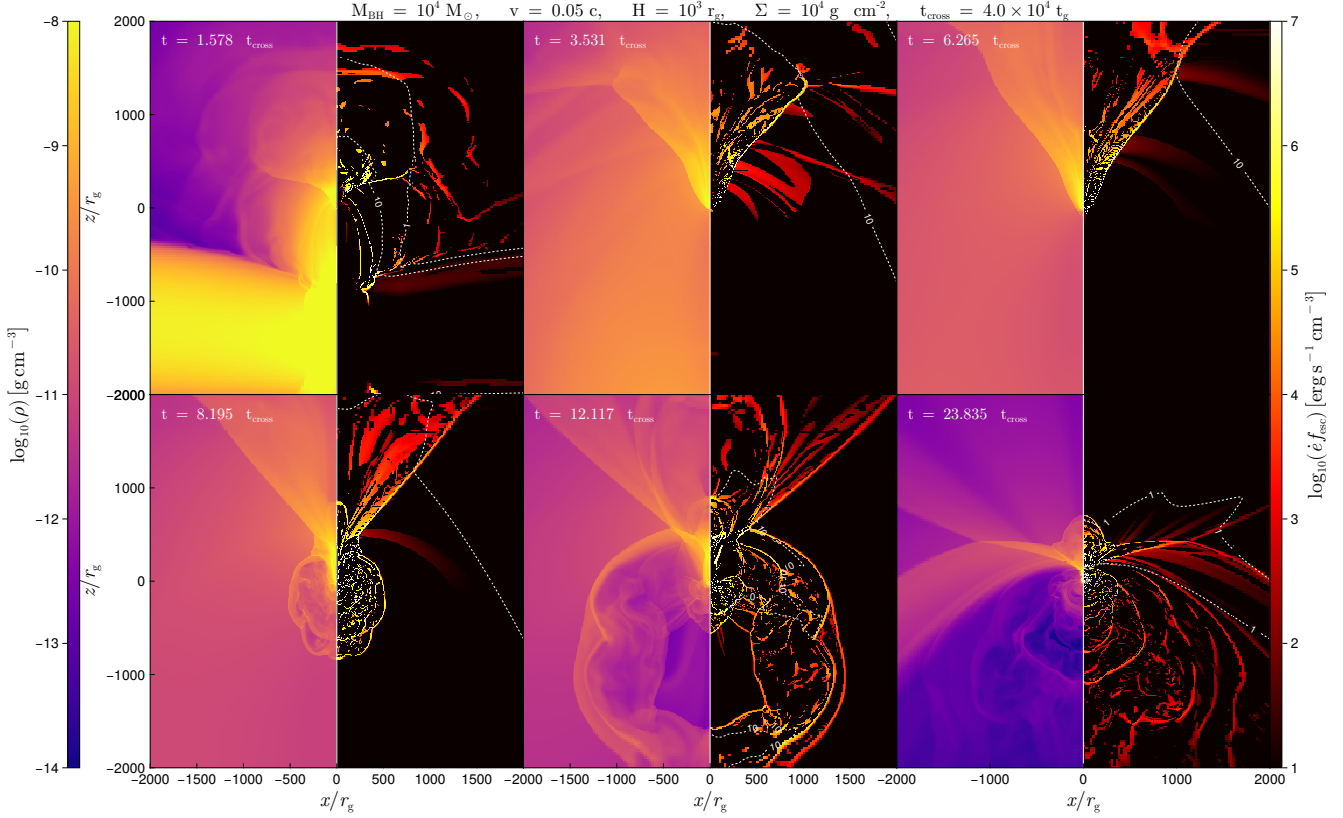


Figure 1. Rest-mass density and energy-generation-rate density weighted by escape fraction together with optical-depth contours at selected times. Snapshots from the $v = 0.05c$, $\Sigma = 10^4 \text{ g cm}^{-2}$ model showing the rest-mass density ρ (left side of each panel) and $\dot{\epsilon} f_{\text{esc}}$ (right side of each panel). The normalization of both quantities corresponds to $m_{\text{BH}} = 10^4 M_{\odot}$. Overlaid curves show contours of optical depth τ computed with the eikonal solver. Each panel corresponds to a different time (as labeled in the figure), illustrating the evolution of the spatial distribution of radiative power that can escape to the observer. Short-timescale fluctuations are unlikely to correspond to observable variability and should not be overinterpreted.

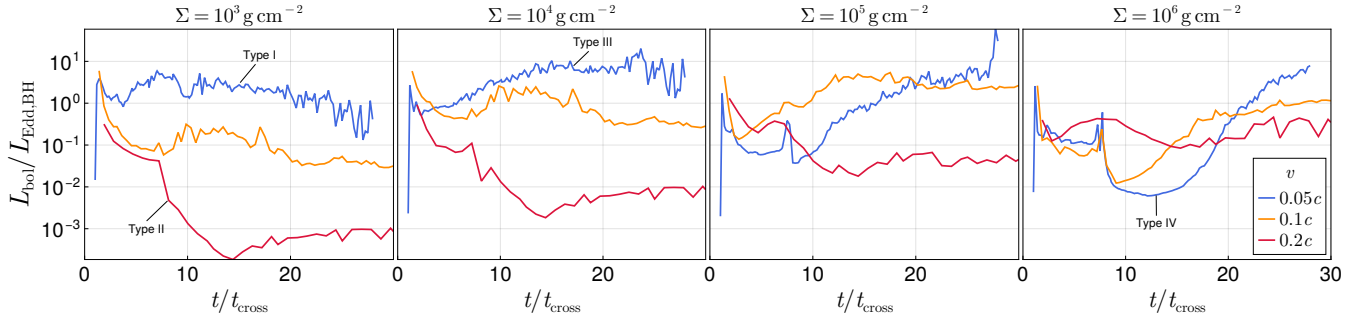


Figure 2. Bolometric luminosities. Bolometric luminosity in units of the Eddington luminosity, $L/L_{\text{Edd,BH}}$, as a function of the dimensionless time t/t_{cross} , for four values of the disk surface density Σ . Colors denote the collision velocity v , as indicated. Representative examples of the four lightcurve morphology types (Types I–IV) are indicated in the panels. Because the horizontal axis is normalized by $t_{\text{cross}} = 2H/v$, the same extent in t/t_{cross} corresponds to a longer physical duration for lower collision velocities.

with velocity ($m_a \propto v^{-4}$; Sec. 2). In several cases, the late phase is as luminous as, or more luminous than, the early phase, despite the overall decline in density, because radiation from the inner hot region becomes progressively less trapped as the optical depth decreases. The light curves show a diversity of temporal behaviors, which we analyze in Sec. 4.2.2. They can also exhibit short-timescale fluctuations that are unlikely to correspond to observable variability and should therefore not be overinterpreted.

Some trends in Fig. 2 can be anticipated from simple scalings. The intercepted mass scales as $m_a = \pi r_a^2 \Sigma \propto \Sigma v^{-4}$ (Sec. 2), implying a rapidly decreasing gas supply at higher v . Departures from monotonic behavior with Σ for $v \leq 0.1c$ are therefore primarily due to radiative suppression through f_{esc} rather than the available gas reservoir alone.

4.2.1 Total radiated energy

In addition to instantaneous luminosities, it is useful to consider the total radiated energy,

$$E_{\text{rad}} = \int L_{\text{bol}}(t) dt. \quad (17)$$

In practice, this integral is evaluated over the simulation interval, $0 < t/t_{\text{cross}} < 30^2$. For the most optically thick models, the reported E_{rad} may be underestimated because the luminosity has not fully declined by the end of the simulation interval.

Fig. 3 shows E_{rad} , normalized by $(m_{\text{BH}}/M_{\odot})^2$, for various velocities and disk densities. The total radiated energy shows a strong dependence on the collision velocity v , decreasing by up to two orders of magnitude between $v = 0.05c$ and $0.2c$ at fixed surface density. For the slowest encounters, peak values reach $E_{\text{rad}} \sim \text{few} \times 10^{39} (m_{\text{BH}}/M_{\odot})^2 \text{ erg}$, while typical energies are reduced to $\sim \text{few} \times 10^{38} (m_{\text{BH}}/M_{\odot})^2 \text{ erg}$ at $v = 0.1c$ and to $\sim 10^{37} - 10^{38} (m_{\text{BH}}/M_{\odot})^2 \text{ erg}$ at $v = 0.2c$. Again, this trend is due to the shorter interaction times and smaller interaction length scale at higher velocities. At fixed velocity, the dependence on surface density is non-monotonic: for low and intermediate velocities, E_{rad} peaks at intermediate density, $\Sigma \sim 10^4 - 10^5 \text{ g cm}^{-2}$, while at the highest velocity the total radiated energy varies more weakly with Σ and peaks at $\Sigma = 10^6 \text{ g cm}^{-2}$.

The total accreted mass onto the secondary across parameter space is within $\sim 40\%$ of $m_a = \pi r_a^2 \Sigma$ (see the right panel of Fig. 4 in L25). The main energy source for radiation is ultimately the binding energy of the accreted matter with respect to the secondary. This motivates defining an estimate of the radiative efficiency as

$$\eta_{\text{rad}} := \frac{E_{\text{rad}}}{m_a c^2}. \quad (18)$$

As shown in Fig. 3, we find $E_{\text{rad}} \ll m_a c^2$ for all parameter combinations explored. The implied efficiencies are small but non-negligible, typically $\eta_{\text{rad}} \sim 10^{-3} - 10^{-2}$, with the largest values obtained for the slowest encounters and lowest surface densities, and a significant decrease towards higher densities, due to optically thicker flows suppressing radiation escape.

4.2.2 Light-curve morphologies

To summarize the diversity of behaviors seen in the simulated light curves, we group them into four qualitative morphological classes based on the relative luminosity of the early and late phases. We identify the following morphological types, which are intended as qualitative descriptors rather than strict classifications:

- *Type I: Plateau.* Sustained emission with modest secular evolution. This occurs when the early escaping luminosity from the BHL shock is followed relatively smoothly by emission from the inner convective region, because photon trapping is not strong enough to produce an interruption between the two components.

- *Type II: Monotonic decay.* This behavior is favored at higher velocities, where the available mass reservoir $m_a \propto \Sigma v^{-4}$ is smaller. In these cases, the BHL-shock-powered early emission fades rapidly and the later convective component remains comparatively weak.

- *Type III: Delayed turn-on.* This occurs when the gas supply is larger than in Type I (low velocities and low/intermediate densities),

² More precisely, the post-processing is applied only to the simulation data at $t > t_{\text{cross}}$, once the black hole has collided with the disk.

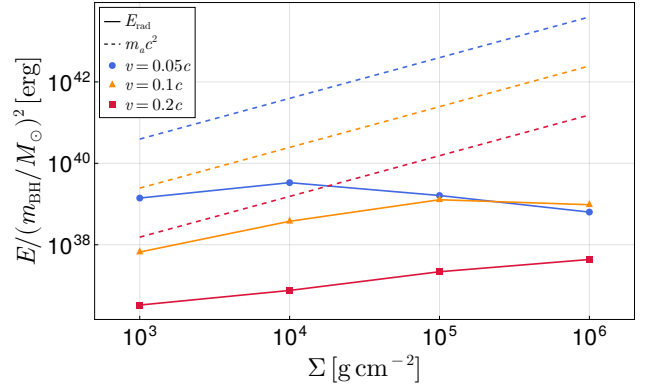


Figure 3. Total radiated energy for $H = 1000 r_g$. Total radiated energy $E_{\text{rad}} = \int L(t) dt$, normalized by $(m_{\text{BH}}/M_{\odot})^2$, shown as a function of disk surface density Σ for three values of the collision velocity v . For each parameter set, the figure also shows the corresponding intercepted rest-mass energy scale $m_a c^2$ (dashed lines), where $m_a = \pi r_a^2 \Sigma$ and $r_a = 2Gm_{\text{BH}}/v^2$. Both quantities are normalized in the same way and are shown for direct comparison of surface density and collision velocity.

so initially radiation escape is suppressed but the emission becomes increasingly visible as the optical depth decreases. The late rise is associated mainly with the gradual emergence of radiation from the inner convective region.

- *Type IV: Dip-and-rebrightening.* A bright early phase followed by a pronounced minimum and a late-time rebrightening. This is most prominent at high Σ , where the early escaping emission is dominated by comparatively outer, lower- τ regions of the BHL shock, while radiation from the inner convective region is initially trapped and only becomes visible after sufficient optical-depth decline.

Two morphological trends are evident. First, increasing v favors Type II behavior: faster impacts intercept less mass ($m_a \propto v^{-4}$) and produce weaker, more rapidly fading transients. Second, increasing Σ favors Type IV behavior. At high surface density, the optical depth is large and the early emission is dominated by the outer portions of the BHL shock. This outer shock fades before the optical depth has decreased sufficiently for radiation from the inner region to escape. An intermediate phase then occurs in which the outer shock has dimmed while the radiation from the inner region remains trapped, producing a pronounced luminosity dip. Once the optical depth drops further, emission from the inner region becomes visible and the system rebrightens. This interpretation will also be present in the band-limited light curves and the spectral evolution discussed in Sec. 4.3.2.

4.3 Spectral dependence

Even though bolometric-luminosity light curves provide insight into the time-dependent energetics of the collision, they can be misleading for observational interpretation. Detectability is inherently frequency-dependent, and therefore a meaningful comparison with observations requires computing the specific luminosity, vL_ν , in relevant electromagnetic bands. Therefore, we now turn to spectral diagnostics of the emission. In Sec. 4.3.1, we show time-averaged spectral energy distributions (SEDs), and in Sec. 4.3.2, we discuss the specific-luminosity light curves at various observing photon frequencies, showing the spectral evolution across parameter space.

4.3.1 Spectral energy distributions

The emission spectra produced by the collision are typically dominated by soft X-rays and exhibit trends with collision velocity, disk surface density, and phase. We first consider time-averaged SEDs, by splitting the simulation time interval in two halves: an early phase corresponding to $0 < t/t_{\text{cross}} < 15$, and a late phase, $15 < t/t_{\text{cross}} < 30$. Fig. 4 shows the time-averaged SEDs, expressed as $\nu L_\nu/L_{\text{Edd,BH}}$, for a representative black hole mass of $m_{\text{BH}} = 10^4 M_\odot$ and a range of black hole velocities and disk surface densities. The time-averaged SEDs are shown as a function of photon energy for both the early and late phases.

The spectra typically rise from optical/UV energies to a broad peak in the soft X-ray band. The peak is typically at $E \sim 1$ keV, with a high-energy tail extending toward $E \sim 10$ keV. At the highest surface densities, however, the early-phase spectrum is softer and peaks around $E \sim 100$ eV.

Three spectral trends are apparent. Increasing velocity, decreasing surface density, and progressing to the late phase all lead to a mild but systematic hardening of the emergent SED. For $v = 0.05c$ and $0.1c$, larger Σ suppresses the high-energy tail above the keV peak, whereas low- Σ models retain substantial emission up to ~ 10 keV. At $v = 0.2c$, this contrast is more pronounced in the late phase: high- Σ models remain comparatively soft, while low- Σ models peak at higher energies and display harder tails.

These trends can be explained by a common cause. The characteristic diffusion time scales as $t_{\text{diff}} \sim \tau \ell_{\text{esc}}/c$, and, at fixed geometry, higher Σ implies larger optical depth and thus longer t_{diff} . When t_{diff} is longer, photons remain coupled to the gas long enough to thermalize efficiently, producing a softer spectrum and suppressing the hard tail. Conversely, lower Σ , higher v (which reduces the gas reservoir and optical depth), and later times (as the flow dilutes) all reduce t_{diff} , allowing photons to escape with less thermalization and yielding a harder emergent spectrum.

In Fig. 5 we show time-averaged SEDs over the whole interval $0 < t/t_{\text{cross}} < 30$, varying black hole mass in the IMBH regime for $v = 0.05c$ and various disk densities. The SEDs soften with increasing mass, with the emission generically dominated by soft X-rays within the IMBH range. The effect is analogous at other collision velocities.

4.3.2 Specific luminosity light curves

Fig. 6 shows the specific luminosity light curves νL_ν for $m_{\text{BH}} = 10^4 M_\odot$ at $E = 10, 10^2, 10^3$, and 10^4 eV. We take the $10^4 M_\odot$ case as representative of the IMBH range because the spectrum depends only weakly on m_{BH} within that range (see Fig. 5 and the scalings discussed in Sec. 4.1).

The emission is generically soft X-ray dominated, consistent with the time-averaged SEDs. For $\Sigma = 10^3\text{--}10^4 \text{ g cm}^{-2}$ and $v \leq 0.1c$, the 1 keV light curve typically reaches the highest peak luminosity and the 100 eV component is typically subdominant. The 10 eV (optical/UV) emission is suppressed by one to two orders of magnitude relative to the soft X-ray band and is therefore unlikely to be observable (see Sec. 5.3). The 10 keV emission is also strongly subdominant in all models.

At higher surface densities, $\Sigma \gtrsim 10^5 \text{ g cm}^{-2}$, there is a more noticeable spectral evolution compared to the lower density models. In these cases the early emission is relatively softer, with the 100 eV band dominating during the initial phase. At later times, however, the 1 keV band rebrightens as the effective optical depth decreases and the inner, hotter region becomes visible. In several high- Σ models, the

peak at 1 keV occurs significantly later than that at 100 eV, indicating a hardening of the spectrum during the flare evolution.

5 DISCUSSION

In this section we discuss the flare duration, compare with emission from the unbound ejecta produced by the collision, and connect the simulation parameter space to astrophysical systems to derive astrophysical implications of our results.

5.1 Flare-duration scaling

A key question for connecting our light curves to observations is how the characteristic flare duration scales with the secondary mass and the collision parameters. Our results show that the accretion-powered component typically persists for $10\text{--}30 t_{\text{cross}}$, i.e. $\sim 10^5\text{--}10^6 t_g$, depending on the model (Sec. 4.2). This is much longer than the disk-crossing time itself, indicating that the flare duration is not set by the geometric crossing alone but by the time required for the post-collision, bound gas reservoir to be accreted and/or to become optically thin enough to radiate efficiently.

A simple estimate can then be obtained by modeling the post-collision phase as the depletion of a bound reservoir of shocked gas. Let the mass of gas that becomes available to feed the post-collision accretion flow scale with the intercepted mass,

$$m_{\text{res}} \sim f_{\text{res}} m_a, \quad (19)$$

where f_{res} is the fraction of the intercepted gas that remains bound and participates in the long-lived accretion (L25 indicates that this fraction is of order unity). Let the characteristic accretion rate during the flare be a fraction $f_{\dot{m}}$ of the characteristic mass flux,

$$\dot{m}_{\text{acc}} \sim f_{\dot{m}} \dot{m}_a, \quad (20)$$

Then the characteristic depletion time is

$$t_{\text{flare}} \sim \frac{m_{\text{res}}}{\dot{m}_{\text{acc}}} \sim \frac{f_{\text{res}}}{f_{\dot{m}}} \frac{m_a}{\dot{m}_a} \sim \chi \frac{r_a}{v} = 2\chi \left(\frac{v}{c}\right)^{-3} t_g, \quad (21)$$

where $\chi := f_{\text{res}}/f_{\dot{m}}$. Importantly, the leading scaling $t_{\text{flare}} \propto m_{\text{BH}} v^{-3}$ is independent of Σ because both m_{res} and \dot{m}_{acc} scale linearly with Σ in this simple picture. Σ primarily modulates the visibility of the emission through photon trapping rather than the depletion timescale itself³.

We can calibrate χ to our light curves using the characteristic duration of the emission for $v \approx 0.05c$, for which $t_{\text{flare}} \sim 30 t_{\text{cross}} \sim 10^6 t_g$. This yields $\chi \sim 60$. With this normalization, Eq. (21) becomes

$$t_{\text{flare}} \approx 10^6 t_g v_{0.05}^{-3} \chi 60, \quad (22)$$

³ If one defines a characteristic luminosity as $L_{\text{char}} \sim E_{\text{rad}}/t_{\text{flare}}$, with $t_{\text{flare}} \sim \chi m_a/\dot{m}_a$ and $E_{\text{rad}} \sim \eta_{\text{rad}} m_a c^2$, then $L_{\text{char}} \sim (\eta_{\text{rad}}/\chi) \dot{m}_a c^2$. Since $\dot{m}_a \propto v^{-1}$, the naive expectation $L_{\text{char}} \propto \dot{m}_a \propto v^{-1}$ holds only if η_{rad}/χ is approximately independent of velocity. Measures of characteristic luminosity extracted from our light curves can show a steeper dependence on v , suggesting that this ratio is not strictly constant across the explored parameter space. This does not necessarily invalidate the duration estimate, but it does indicate that the simple argument may not by itself fix a characteristic luminosity. Further clarification of this point is warranted, and will likely require radiation-hydrodynamics simulations to assess more carefully the relation between gas supply and emergent luminosity.

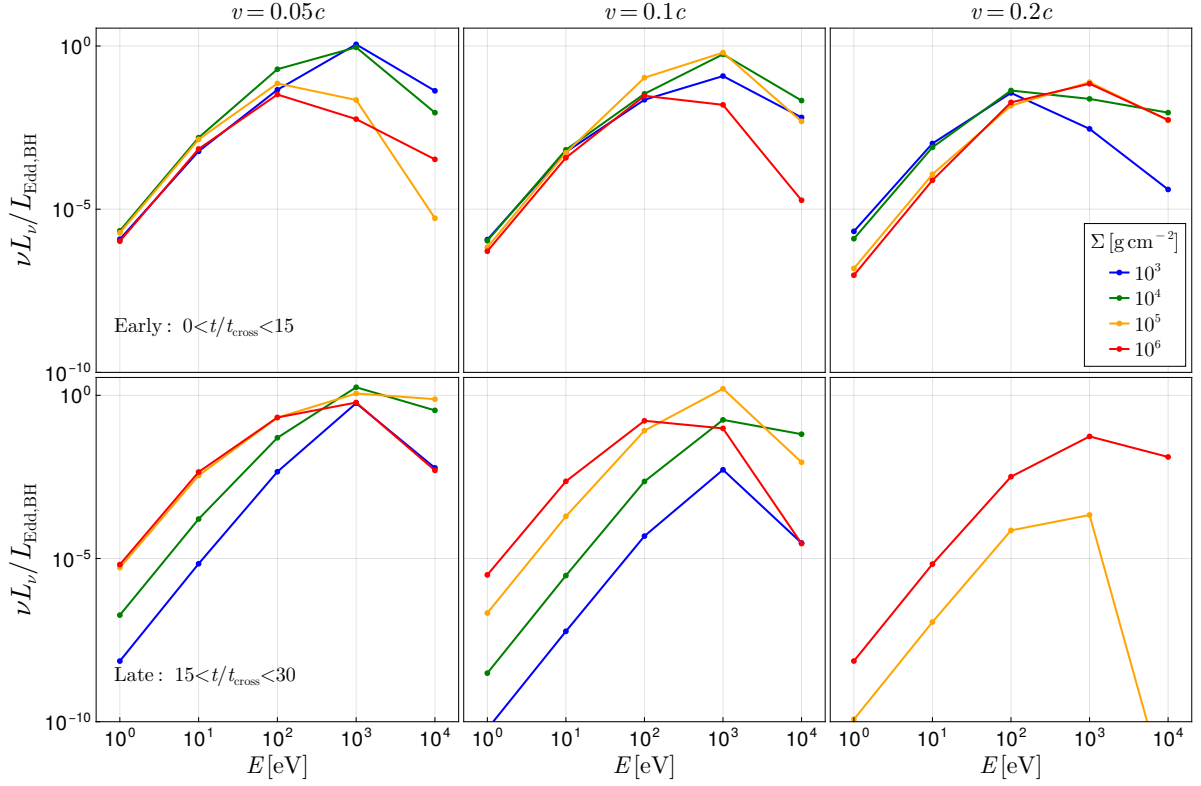


Figure 4. Time-averaged SEDs for $m_{\text{BH}} = 10^4 M_{\odot}$. Columns correspond to black hole velocities $v = 0.05c, 0.1c,$ and $0.2c$, while the top and bottom panels show the early and late phases, respectively. Colors denote the disk surface density Σ . The emission is generically dominated by the soft X-ray band. The curves for $\Sigma = 10^3$ and 10^4 g cm^{-2} at $v = 0.2c$ in the late phase are not shown because the gas becomes very optically thin, invalidating the assumptions underlying our local temperature estimate.

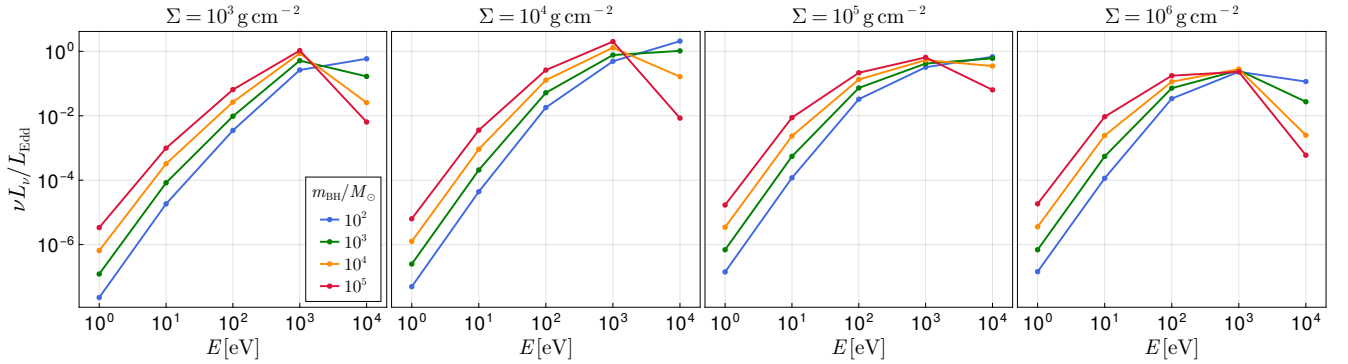


Figure 5. Time-averaged SEDs for $v = 0.05c$, varying black hole mass. Time-averaged spectral energy distributions $\nu L_{\nu}/L_{\text{Edd}}$ shown as a function of photon energy E . Columns correspond to disk surface densities $\Sigma = 10^3, 10^4, 10^5,$ and 10^6 g cm^{-2} . Colors denote the black hole mass m_{BH} .

where $\chi_{60} := \chi/60$, or, in physical units,

$$t_{\text{flare}} \approx 13.6 \text{ h } m_{\text{BH},4} v_{0.05}^{-3} \chi_{60}. \quad (23)$$

Thus, for IMBH secondaries the duration of the accretion-powered episode is naturally of order hours to days, with a steep sensitivity to the collision velocity. Variations in the dimensionless disk scale height h would enter primarily through the early dynamics (at the shorter timescale t_{cross}).

The scaling derived above assumes that the flare duration is set by the depletion time of the reservoir. This requires that photons

produced in the accretion flow can escape on a timescale shorter than the depletion time. In sufficiently optically thick flows, however, the photon diffusion time can become comparable to or longer than the depletion time. We find that this situation arises primarily at the highest surface densities explored ($\Sigma \gtrsim 10^5 \text{ g cm}^{-2}$), where the optical depth of the post-collision flow is largest. When $t_{\text{diff}} \gtrsim t_{\text{flare}}$, the simple scaling $t_{\text{flare}} \propto v^{-3}$ may therefore be modified. A more detailed treatment of this regime lies beyond the scope of the present work.

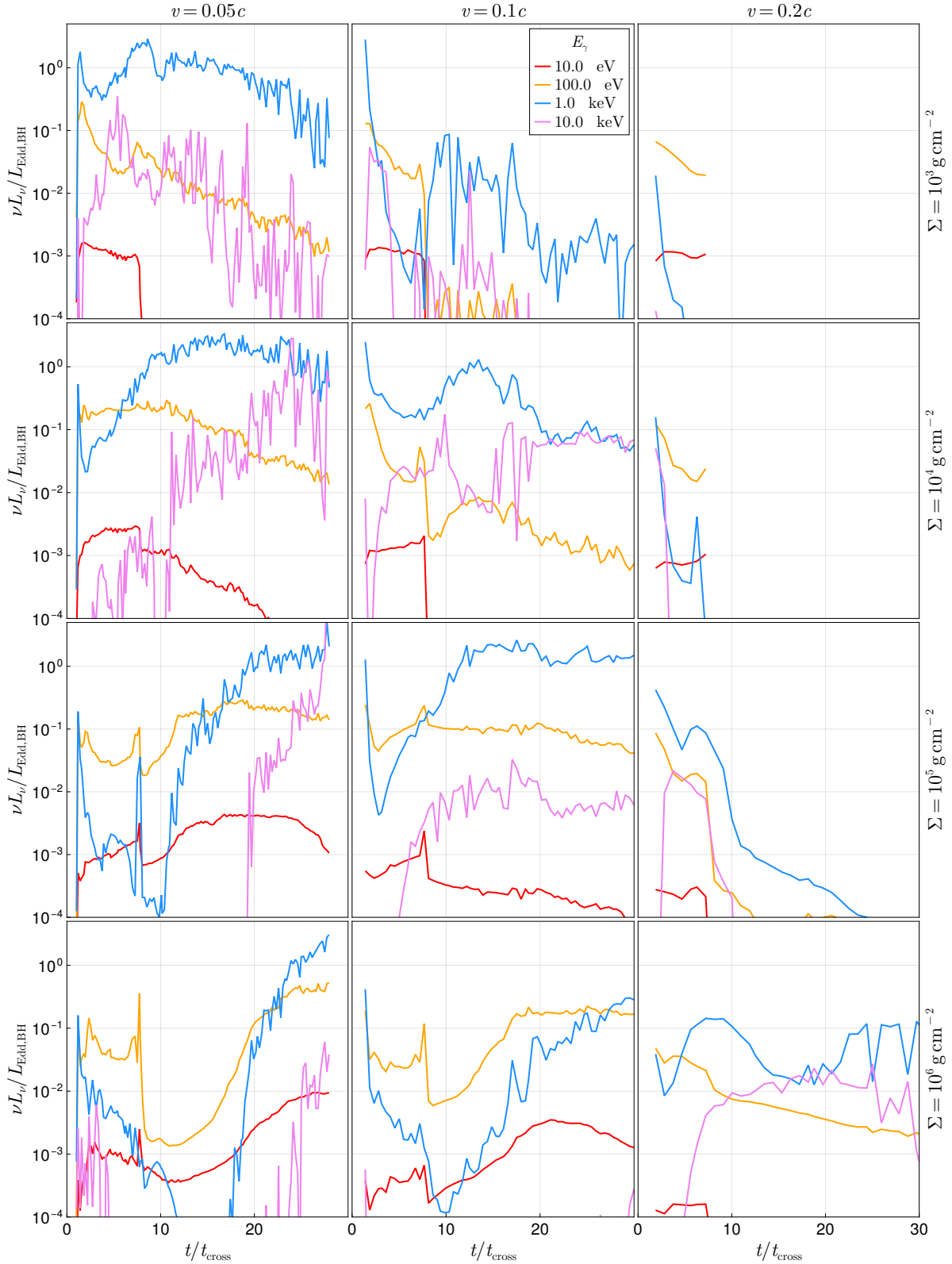


Figure 6. Specific luminosity light curves for $m_{\text{BH}} = 10^4 M_{\odot}$. Specific luminosity $\nu L_{\nu}/L_{\text{Edd,BH}}$ shown as a function of time for simulations with $H = 1000 r_g$. Columns correspond to black hole velocities $v = 0.05c$, $0.1c$, and $0.2c$, while rows correspond to disk surface densities $\Sigma = 10^3, 10^4, 10^5$, and 10^6 g cm^{-2} . Colors denote the observing energies, $E = 10, 100, 10^3$, and 10^4 eV . Because the horizontal axis is normalized by $t_{\text{cross}} = 2H/v$, the same extent in t/t_{cross} corresponds to a longer physical duration for lower collision velocities. Short-timescale fluctuations in the curves are unlikely to correspond to observable variability and should not be overinterpreted.

5.2 Relation to ejecta-powered emission and multi-component flares

The unbound ejecta produced during the collision may power electromagnetic emission as it expands and cools (Lehto & Valtonen 1996; Ivanov et al. 1998; Franchini et al. 2023; Linial & Metzger 2023, L25), a component not explicitly modeled in our present framework. Black hole–disk collisions can give rise to structured, multi-peaked flares produced by the superposition of the long-lived accretion-powered component modeled above and the prompt radiation from the unbound ejecta. Based on Eq. (29) of L25 for the peak timescale of ejecta emission, and adopting the estimate from Sec. 5.1 for the accretion-powered flare duration, the ejecta peak time is typically earlier than the accretion-powered flare duration by a factor of

$$\frac{t_{\text{peak,ej}}}{t_{\text{flare}}} \sim 0.06 \Sigma_4^{1/2} v_{0.05}^{1/2} \left(\frac{v_{\text{ej}}}{v}\right)^{-1/2} \left(\frac{m_{\text{ej}}}{0.1 m_a}\right)^{1/2} \chi_{60}^{-1}, \quad (24)$$

where m_{ej} and v_{ej} are the characteristic ejecta mass and velocity, respectively, scaled to the typical values measured in the simulations. The peak luminosity of the ejecta is estimated in L25 as $L_{\text{peak,ej}} \sim L_{\text{Edd,BH}}$, essentially independent of parameters. Therefore, the observed flare may consist of a brief precursor from the ejecta followed by a broader accretion-powered component. In some regimes, the accretion-powered emission alone already produces two maxima, such that the addition of an ejecta precursor may yield a three-component structure.

Fig. 7 provides a schematic representation of this phenomenology at relatively low encounter velocities ($v \lesssim 0.05c$), where the accretion-powered emission is strongest, and increasing surface density enhances dip-and-rebrightening morphology. The intermediate-time minimum deepens and the late-time maximum becomes more pronounced as Σ increases, consistent with stronger photon trapping and delayed emergence of radiation from the inner convective region.

If the disk surface density evolves with time, the flare morphology may evolve accordingly. In a tidal disruption event, for example, the disk mass is limited by the initially bound debris. As this material accretes onto the primary over a timescale of years, the effective surface density is likely to decrease. One may then speculate a transition from structured, soft X-ray flares with multiple temporal peaks at high Σ toward smoother, more monotonic profiles as the disk becomes depleted. However, note that Mummery (2025) argues that this picture could be challenged for QPEs following TDEs, because for very massive IMBHs (with mass ratio to the primary $\gtrsim 0.1$), the finite mass of a debris disk formed from the initially bound stellar material may be drained too quickly by repeated impacts.

5.3 Mapping the predicted flares to astrophysical systems

To connect the parameter space explored in this work to astrophysical systems, we relate the secondary black hole velocity v to the Keplerian orbital velocity and the disk surface density Σ to the properties of a standard thin accretion disk (Shakura & Sunyaev 1973) around the primary. This mapping allows us to relate the flare duration to the recurrence period of the emission and to compare the flare luminosity to that of the underlying quiescent disk.

5.3.1 Orbital parameters and flare duration

We define the QPE recurrence period as $P_{\text{QPE}} := P_{\text{orb}}/2$, where P_{orb} is the orbital period, assuming a spherical orbit. This corresponds to the interval between successive disk crossings, and assumes that

each crossing produces a visible flare. For a circular Keplerian orbit around a primary of mass M_c , the orbital radius can be expressed as

$$R = \left(G M_c P_{\text{QPE}}^2 / \pi^2\right)^{1/3} \approx 314 R_g M_{c,6}^{-2/3} P_{\text{QPE,d}}^{2/3}, \quad (25)$$

where $R_g := GM_c/c^2$ is the gravitational radius of the primary, $M_{c,6} := M_c/10^6 M_\odot$, and $P_{\text{QPE,d}} := P_{\text{QPE}}/1 \text{ d}$. The corresponding orbital velocity of the secondary is

$$v = (GM_c/R)^{1/2} \approx 0.056c M_{c,6}^{1/3} P_{\text{QPE,d}}^{-1/3}. \quad (26)$$

Combining Eq. (26) with the relation $t_{\text{flare}} \propto m_{\text{BH}} v^{-3}$ from Eq. (23), we obtain

$$\frac{t_{\text{flare}}}{P_{\text{QPE}}} \approx 0.4 q_{-2} \chi_{60}. \quad (27)$$

where $q := m_{\text{BH}}/M_c$ is the mass ratio, and $q_{-2} := q/10^{-2}$.

5.3.2 Thin-disk surface density scalings

The disk surface density at the crossing radius depends on the local pressure regime of the disk. In the outer regions of a Shakura–Sunyaev disk⁴ the pressure is dominated by gas, yielding (Frank et al. 2002)

$$\Sigma_{(\text{gas})} \approx 1.2 \times 10^5 M_{c,6}^{3/5} P_{\text{QPE,d}}^{-2/5} \dot{m}_{-1}^{3/5} \alpha_{-1}^{-4/5} \eta_{-1}^{-3/5} \text{ g cm}^{-2}, \quad (28)$$

where $\dot{M}_{\text{Edd,c}} := L_{\text{Edd,c}}/(\eta c^2)$, $L_{\text{Edd,c}}$ is the Eddington luminosity of the primary, η is the radiative efficiency of the disk, $\dot{m} := \dot{M}_c/\dot{M}_{\text{Edd,c}}$, $\dot{m}_{-1} := \dot{m}/0.1$, $\alpha_{-1} := \alpha/0.1$, and $\eta_{-1} := \eta/0.1$. In the innermost, radiation-pressure dominated region the surface density instead scales as

$$\Sigma_{(\text{rad})} \approx 1.1 \times 10^5 M_{c,6}^{-1} P_{\text{QPE,d}} \dot{m}_{-1}^{-1} \alpha_{-1}^{-1} \eta_{-1} \text{ g cm}^{-2}. \quad (29)$$

5.3.3 Band-dependent visibility against the quiescent disk

To assess in which bands the flare may be visible above the quiescent emission of the primary disk, we compare the simulated specific luminosities with a simple estimate of the thin-disk emission. Writing the quiescent disk luminosity as

$$L_{\text{disk}} \approx \dot{m} L_{\text{Edd,c}} \approx 10 \dot{m}_{-1} q_{-2}^{-1} L_{\text{Edd,BH}}, \quad (30)$$

where $L_{\text{Edd,c}}$ is the Eddington luminosity of the primary, and the characteristic inner-disk temperature as

$$k_B T_{\text{disk}} \sim k_B \left(\frac{3GM_c \dot{M}_c}{8\pi\sigma R_{\text{ISCO}}^3}\right)^{1/4} \approx 30\text{--}60 \text{ eV } \dot{m}_{-1}^{1/4} M_{c,6}^{-1/4}, \quad (31)$$

we can obtain order-of-magnitude estimates for the quiescent specific luminosity at different photon energies. Near the thermal peak of the thin disk, we can write

$$\frac{\nu L_{\nu,\text{flare}}}{\nu L_{\nu,\text{disk}}} \approx \frac{\nu L_{\nu,\text{flare}}}{L_{\text{disk}}} \approx 0.1 \left(\frac{\nu L_{\nu,\text{flare}}}{L_{\text{Edd,BH}}}\right) \dot{m}_{-1}^{-1} q_{-2}. \quad (32)$$

At $E \sim 10 \text{ eV}$, which lies near the thermal peak of the thin disk, our models typically give $\nu L_{\nu,\text{flare}}(10 \text{ eV}) \lesssim 10^{-3} L_{\text{Edd,BH}}$. The flare is therefore expected to be strongly outshone in the optical/UV band for all astrophysically relevant parameters. However, this does not exclude the possibility of a delayed UV counterpart, as recently

⁴ We only consider regimes where the opacity is dominated by electron scattering, neglecting the outermost region where free–free opacity dominates.

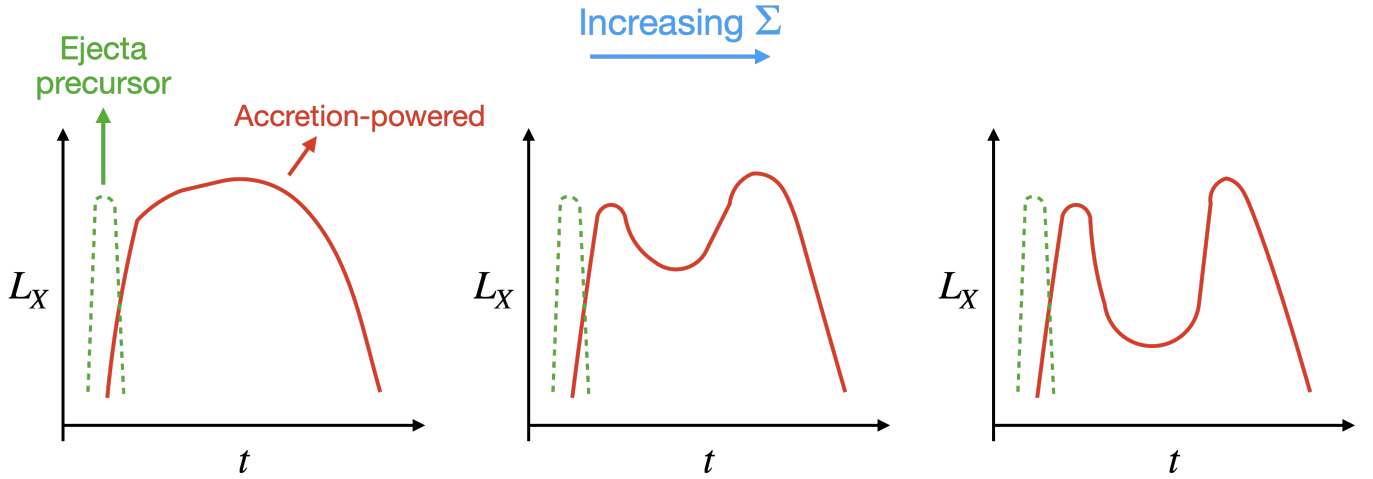


Figure 7. Schematic illustration of structured flare morphologies from black hole–disk collisions at relatively low velocities, $v \lesssim 0.05c$. The dashed green curve represents a prompt ejecta-powered precursor, while the solid red curves illustrate the accretion-powered emission. The curves are illustrative and not derived from a quantitative light-curve model.

discovered (Guo et al. 2026) in the QPE source “Ansky” (Sánchez-Sáez et al. 2024; Hernández-García et al. 2025a; Chakraborty et al. 2025b; Zhu et al. 2025; Hernández-García et al. 2025b; Chakraborty et al. 2026), if the direct X-ray flare is reprocessed elsewhere, for example in the outer regions of a warped disk.

At $E \sim 100$ eV, only a factor of a few above the characteristic disk temperature, the simulated flares reach $\nu L_\nu(100 \text{ eV}) \sim 0.1 L_{\text{Edd,BH}}$, implying that direct visibility in this band may be possible only for $\dot{m}_{-1} \lesssim 0.01 q_{-2}$, i.e., for example, for $q \approx 10^{-2}$ and $\dot{m} \lesssim 10^{-3}$.

At $E \sim 1$ keV the quiescent thin-disk emission lies deep in the Wien tail ($E/kT_{\text{disk}} \sim 20\text{--}30$) and is therefore exponentially suppressed, whereas the flare typically reaches $\nu L_{\nu,\text{flare}}(1 \text{ keV}) \sim 0.1\text{--}10 L_{\text{Edd,BH}}$. Consequently, the accretion-powered flare should be most readily detectable in the soft X-ray band even when its bolometric luminosity is smaller than that of the underlying disk.

5.3.4 Qualitative flare regimes in the (P_{QPE}, M_c) plane

Fig. 8 shows the parameter space explored in this work in the plane of P_{QPE} and M_c , for representative values $\dot{m} = 0.1$ and 0.01 , $\alpha = 0.1$ and 0.01 , and assuming $\eta = 0.1$. Based on our results, we identify three broad physical regimes in parameter space, defined by the two quantities that most strongly control the flare properties: the collision velocity v , which sets the intercepted gas mass and therefore the available energy reservoir, and the disk surface density Σ , which primarily regulates photon trapping and spectral evolution. The chosen boundaries should not be interpreted as sharp physical transitions, but rather as approximate guides to the qualitative behaviors inferred from our results.

- **Region I:** ($v \gtrsim 0.1c$). At high collision velocities the accretion radius is small and the intercepted gas mass is strongly reduced (because $m_a \propto v^{-4}$). As a result, the flares are generally faint and short-lived. Their light curves have typically simple morphologies⁵,

⁵ Except at the very highest densities $\Sigma \approx 10^6 \text{ g cm}^{-2}$ where dip-and-rebrightening behavior starts to be apparent. For simplicity, we do not consider an additional class for this case.

with spectra peaking around 1 keV and showing little spectral evolution.

- **Region II:** ($v \lesssim 0.1c$ and $\Sigma \gtrsim 3 \times 10^4 \text{ g cm}^{-2}$). Here the gas reservoir remains large, but the optical depth is sufficiently high that photon trapping strongly affects the observed emission. The flares can still be luminous, but their early emission is softer, often peaking near ~ 100 eV, and the spectrum hardens with time as radiation from the inner hotter region becomes visible. The light curves show dip-and-rebrightening behavior.

- **Region III:** ($v \lesssim 0.1c$ and $\Sigma \lesssim 3 \times 10^4 \text{ g cm}^{-2}$). In this regime the secondary intercepts a large gas reservoir, while the optical depth is moderate enough that radiation can escape relatively promptly. The resulting flares are typically luminous, again with simple morphology, peaking around ~ 1 keV and with little spectral evolution.

In Fig. 8, the dashed curve corresponds to $v = 0.1c$ obtained from Eq. (26) assuming a circular Keplerian orbit. It approximately separates a high-velocity regime, where flares are faint, from a slower-interaction regime, where flares are luminous. Colored curves show contours of constant surface density Σ derived from the thin-disk scalings above. Because Σ scales on (M_c, P_{QPE}) with opposite signs in the gas- and radiation-pressure regimes, the constant- Σ contours change slope across the transition between these branches, producing the wedged shapes visible in Fig. 8. The shaded regions illustrate Regions I, II and III in pink, cyan, and yellow, respectively.

The conditions defining each regime can be recast in terms of P_{QPE} and M_c . For example, the defining condition of Region I ($v \gtrsim 0.1c$) corresponds to

$$\text{(Region I)} \quad P_{\text{QPE,d}} \lesssim 0.17 M_{c,6}. \quad (33)$$

Because the density contours change slope across the pressure transition, the Σ conditions cannot in general be written as a simple scaling of P_{QPE} and M_c . However, for typical parameters $\dot{m} \sim 0.01\text{--}0.1$ and $\alpha \sim 0.01\text{--}0.1$, and within the mass and period range shown in Fig. 8, the II/III transition lies entirely within the gas-pressure dominated regime. In that case, we can use Eq. (28) to give the conditions

$$\begin{aligned} \text{(Region II)} \quad & P_{\text{QPE,d}} \gtrsim 0.17 M_{c,6}, \\ & P_{\text{QPE,d}} \lesssim 2 M_{c,6}^{3/2} \dot{m}_{-1}^{3/2} \eta_{-1}^{-3/2} \alpha_{-1}^{-2}. \end{aligned} \quad (34)$$

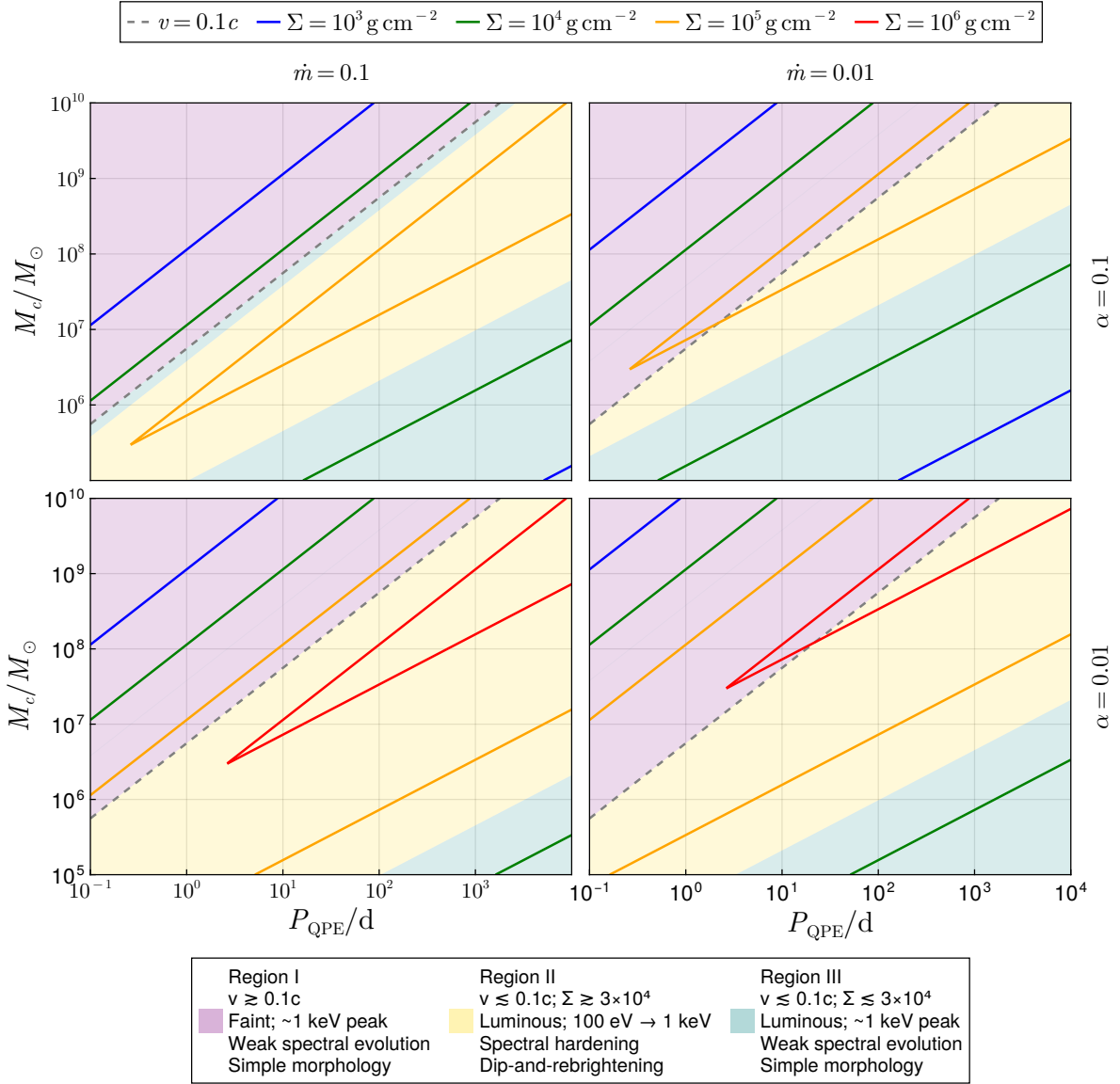


Figure 8. Regions of parameter space with qualitatively different flare properties. The panels show the plane of QPE recurrence period P_{QPE} and primary mass M_c for representative values of the accretion rate $\dot{m} = 0.1$ and 0.01 and viscosity parameter $\alpha = 0.1$ and 0.01 , assuming a radiative efficiency $\eta = 0.1$. The dashed curve corresponds to a Keplerian velocity $v = 0.1c$ for a circular orbit of period $P_{\text{orb}} = 2P_{\text{QPE}}$. Colored curves show contours of constant disk surface density Σ derived from the Shakura–Sunyaev thin-disk scalings in the gas- and radiation-pressure dominated regimes. The change of slope of the contours reflects the transition between these regimes. Shaded regions indicate the approximate parameter ranges where the simulations predict different qualitative emission behaviors (see Sec. 5.3).

$$\begin{aligned}
 \text{(Region III)} \quad P_{\text{QPE},d} &\gtrsim 0.17M_{c,6}, \\
 P_{\text{QPE},d} &\gtrsim 2M_{c,6}^{3/2} \dot{m}_{-1}^{3/2} \eta_{-1}^{-3/2} \alpha_{-2}^{-2},
 \end{aligned} \tag{35}$$

5.4 Implications for known QPE sources

An interesting feature of the depletion-time estimate is that, once the collision velocity is related to the orbital period through Eq. (26), it yields $t_{\text{flare}} \propto P_{\text{QPE}}$. In this sense, the model gives a scaling with recurrence period consistent with the observed trend in known QPEs. For primaries of order $10^7 M_\odot$ and secondaries in the range $m_{\text{BH}} \sim \text{few} \times 10^4 M_\odot$, the estimate gives $t_{\text{flare}}/P_{\text{QPE}} \sim 0.05\text{--}0.2$,

comparable to the typical QPE duty cycle. A caveat to this argument is that the scaling derived in Sec. 5.1 assumes that the flare duration is set by the depletion time of the bound gas reservoir. As discussed there, at the highest surface densities explored ($\Sigma \gtrsim 10^5 \text{ g cm}^{-2}$) the simple scaling $t_{\text{flare}} \propto v^{-3}$ leading to $t_{\text{flare}} \propto P_{\text{QPE}}$ is likely to be modified. Therefore, this correspondence should be regarded as suggestive rather than definitive.

Energetic considerations nevertheless indicate that black hole–disk collisions are unlikely to account for the majority of QPEs. It has been argued that such encounters may be energetically insufficient (Linial & Metzger 2023) and may also be limited by the finite mass budget of TDE disks (Mummery 2025). In particular, Linial & Metzger (2023) estimates the maximum radiated energy

per collision assuming that the accretion rate onto the secondary is limited by the Bondi rate. They note that the inferred QPE event rate (Arcodia et al. 2024b; Chakraborty et al. 2025a) would require a large population of massive secondaries in galactic nuclei, implying such rapid SMBH growth by mergers with IMBHs that the observation of $\sim 10^6 M_\odot$ SMBHs would be unlikely. Our results are broadly consistent with these arguments. We find total radiated energies $E_{\text{rad}} \sim 10^{37} - 10^{39} (m_{\text{BH}}/M_\odot)^2$ erg across our parameter space, comparable to the estimates in Linial & Metzger (2023). However, these energetic arguments do not rule out the possibility that a subset of QPEs, or other repeating transients yet to be identified, could be powered by such collisions.

Particularly interesting tests may come from sources that show evidence for multiple flare components. In this respect, eRO-QPE1 (Arcodia et al. 2021) appears especially interesting for the black hole–disk collision scenario. This source shows evidence for complex eruptions that can be interpreted as partially superposed flares (Arcodia et al. 2022), and recent long-term monitoring suggests that EMRI–disk collision models are broadly consistent with its observed timing properties (Chakraborty et al. 2024). For its recurrence time of ~ 18.5 h and a central mass in the $\sim 10^5 - 10^6 M_\odot$ range, Eq. (26) gives a Keplerian velocity $v \sim 0.04 - 0.06c$, well within the slow-collision regime where our models predict the most luminous and longest-lived accretion-powered flares. Moreover, the observed duty cycle, $t_{\text{flare}}/P_{\text{QPE}} \approx 7.6/18.5 \approx 0.4$, is broadly consistent with Eq. (27) for a mass ratio $q \sim 10^{-2}$, corresponding to an IMBH secondary. In this sense, the characteristic timescale and luminosity scale of eRO-QPE1 are consistent with the black hole–disk collision picture presented here. However, the long-term variations and irregular overlap of eruptions reported in this source suggest that additional ingredients beyond the local approximation of our framework may be required, including orbital precession and the global structure of the disk.

More extreme structured QPEs such as the recently discovered in J2344 (Baldini et al. 2026), five years after a TDE-like flare (Homan et al. 2023; Goodwin et al. 2024), are harder to accommodate in this picture. J2344 exhibits broad flares accompanied by a crest of narrower, hotter flares, an unprecedented phenomenology within the current QPE sample. For a recurrence time of ~ 12 h and a central mass $M_c \sim 10^7 M_\odot$, Eq. (26) gives $v \approx 0.15c$, toward the high-velocity end of the parameter space explored here, where the intercepted gas mass is strongly reduced and the flares tend to be fainter and shorter-lived. Matching the observed hour-scale durations and luminosity scale would require a secondary of at least a few $\times 10^4 M_\odot$, for which the corresponding gravitational-wave inspiral time would be only of order $\sim 10 - 90$ yr. Observing a system in this short-lived configuration may therefore be unlikely. However, there is evidence that J2344 may be a recently faded AGN, which could enhance both TDE and EMRI rates (Jiang & Pan 2025). In such environments, the probability of detecting a system with this short lifetime may be significantly increased.

5.5 Implications for OJ 287

OJ 287 is one of the best-known candidates for a supermassive black-hole binary in which a secondary periodically impacts the accretion disk of a much more massive primary. In the standard impact model (e.g. Lehto & Valtonen 1996; Valtonen et al. 2008), the primary mass is $M_c \sim 10^{10} M_\odot$ and the secondary mass is $\sim 10^8 M_\odot$, with an orbital period of ~ 9 yr (rest frame) and high eccentricity ($e \sim 0.6 - 0.7$). The circular Keplerian estimate of Eq. (26) gives $v \approx 0.07c$.

The observed optical outbursts of OJ 287 reach luminosities of order $L \sim 10^{46} - 10^{47} \text{ erg s}^{-1}$. In our models the luminosity scale typically reaches $\sim 1 - 10 L_{\text{Edd,BH}}$, implying a secondary mass $m_{\text{BH}} \sim 10^8 M_\odot$, consistent with the masses invoked in binary-SMBH interpretations of OJ 287. However, combining this mass estimate with the flare-duration scaling derived in Sec. 5.1, $t_{\text{flare}} \approx 13.6 \text{ h } m_{\text{BH},4} v_{0.05}^{-3}$, gives a characteristic duration $t_{\text{flare}} \sim \text{few years}$ for $m_{\text{BH}} \sim 10^8 M_\odot$ and $v \sim 0.07c$. This is substantially longer than the observed weeks-to-months duration of the major optical outbursts in OJ 287. This tension is in line with previous arguments in Linial & Metzger (2023).

5.6 Detectability and observational prospects

Combining the thin-disk mapping of Sec. 5.3 with the flare-duration estimate of Sec. 5.1 allows us to identify where QPE-like black hole–disk collision flares are most likely to be observable in parameter space. In Fig. 9, we show a diagram in the $(P_{\text{QPE}}, m_{\text{BH}})$ plane, complementary to Fig. 8. At fixed M_c , increasing P_{QPE} lowers the orbital velocity and therefore increases the intercepted gas mass, favoring more luminous flares. Increasing m_{BH} raises the luminosity scale but also lengthens the flare duration and shortens the gravitational-wave inspiral time. The most favorable systems are therefore expected in an intermediate region of parameter space: outside the high-velocity regime $v \gtrsim 0.1c$, and not so far toward large m_{BH} that successive flares overlap or the inspiral time becomes very short.

A useful guide is provided by Eq. (27), $t_{\text{flare}}/P_{\text{QPE}} \approx 0.4 q_{-2} \chi_{60}$. When this ratio is small, individual impacts can produce well-separated QPE-like flares. As the ratio approaches unity, consecutive flares may overlap, leading instead to lower-contrast quasi-periodic or sustained variability. Our results do not allow us to describe that regime reliably, because they are based on a local approximation and do not include the global structure of the disk or the orbit of the secondary. In this sense, the most favorable QPE-like candidates are expected in Regions II–III with moderate mass ratios, producing luminous, temporally distinct flares, while Region I sources should generally be fainter and therefore harder to detect unless they are unusually nearby.

Our results also indicate that wide-field soft-X-ray monitoring is the natural discovery channel for these events. In the IMBH regime, the flares are expected to last hours to days and to peak mainly in the $\sim 0.1 - 1$ keV band. Einstein Probe (Yuan et al. 2022) is particularly useful to discovering such events, whereas XMM–Newton (Jansen et al. 2001) is well suited to pointed follow-up. Among future prospects, *NewAthena* (Barcons et al. 2017) should further improve the follow-up of these systems, while the wide-field mission concept THESEUS (Amati et al. 2021) may also become relevant for discovery if realized.

6 CONCLUSIONS

In this work we studied the electromagnetic signatures of black hole–disk collisions by applying a post-processing framework of radiative processes to relativistic hydrodynamics simulations. Our main conclusions are as follows:

- The observable emission is dominated by the long-lived, post-collision accretion flow onto the secondary black hole, rather than by cooling of the unbound ejecta. This accretion-powered component can be highly super-Eddington, and the luminosity can reach several times $L_{\text{Edd,BH}}$.

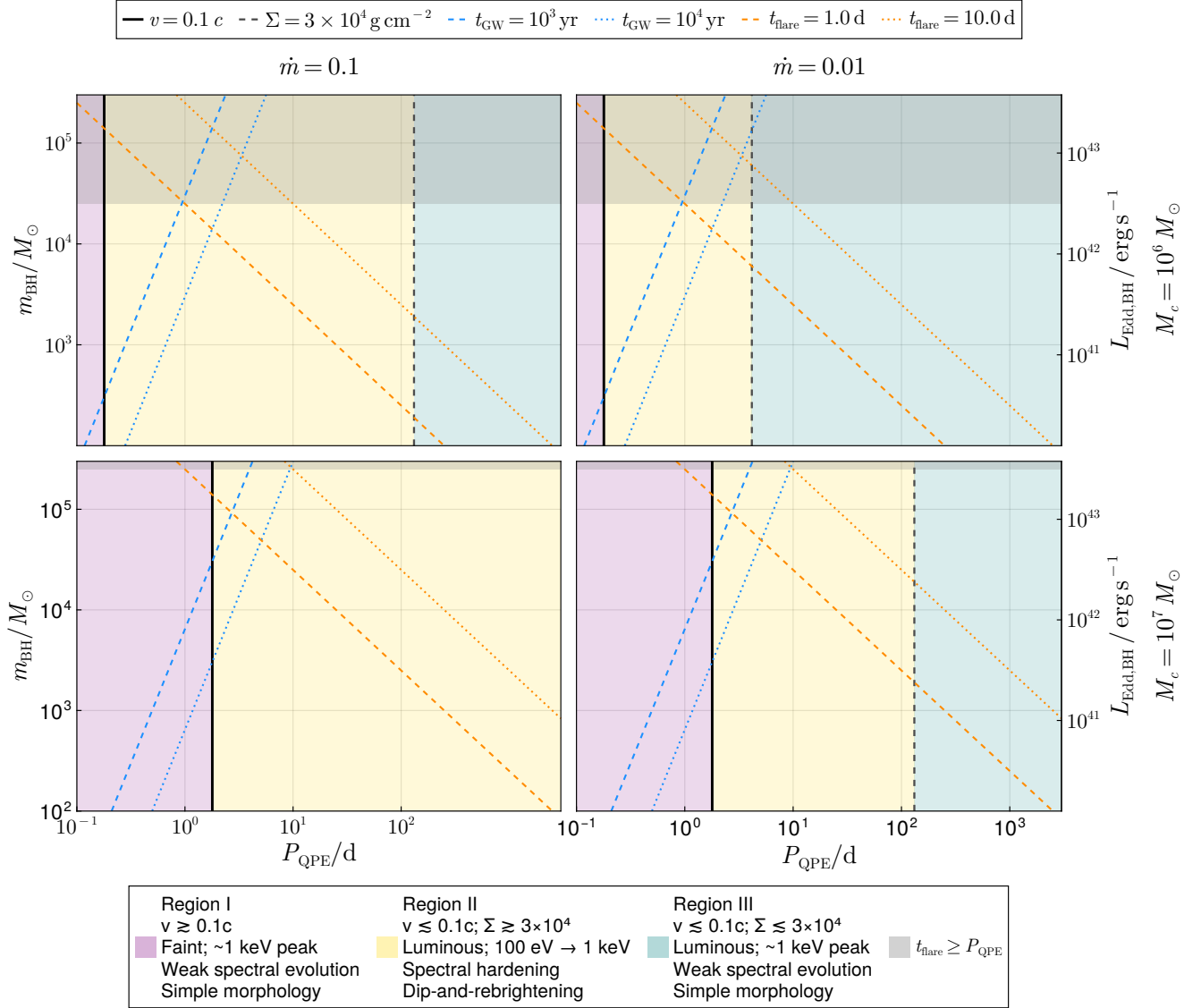


Figure 9. Parameter space in the $(P_{\text{QPE}}, m_{\text{BH}})$ plane. The panels show the recurrence period P_{QPE} and secondary black-hole mass m_{BH} for representative values of the primary mass M_c and accretion rate \dot{m} , assuming the Shakura–Sunyaev disk scalings of Sec. 5.3, with $\alpha = 0.05$ and $\eta = 0.1$. Colored regions indicate the three qualitative flare regimes defined from Fig. 8. Colored curves show contours of flare duration t_{flare} from the analytic estimate of Eq. (23), while blue curves show contours of gravitational-wave inspiral time t_{GW} . The gray shaded regions mark where $t_{\text{flare}} \geq P_{\text{QPE}}$, implying the emission is not QPE-like and our framework does not apply.

- The emission is generically dominated by soft X-rays, typically peaking near $E \sim 1$ keV.

- The overall energetics depends strongly on the collision velocity because the intercepted gas mass scales as $m_a \propto v^{-4}$. Relatively lower-velocity encounters therefore produce substantially more luminous and more energetic flares, with $E_{\text{rad}} \sim 10^{37} - 10^{39} (m_{\text{BH}}/M_{\odot})^2$ erg, over the explored parameter space.

- The disk surface density mainly regulates photon trapping and thus the temporal and spectral evolution of the flare. High- Σ models show softer early emission and more pronounced non-monotonic light curves, including dip-and-rebrightening behavior.

- A depletion-time estimate calibrated to our results suggests characteristic durations of hours to days for IMBH secondaries, with $t_{\text{flare}} \propto P_{\text{QPE}}$ (Eqs. (23) and (27)). This connection is suggestive for

QPE-like transients, although the scaling may not hold in the most optically thick cases.

Our results also clarify the conditions under which black hole–disk collisions may produce observable transients in galactic nuclei. Because the intercepted gas mass decreases steeply with increasing collision velocity, luminous, long-duration flares are favored in relatively slow encounters, while high-velocity collisions are expected to produce weaker flares. In the IMBH regime explored here, the most promising discovery channel is wide-field soft-X-ray monitoring.

Several limitations should be kept in mind. The underlying hydrodynamics simulations neglect radiation forces and cooling, the radiative post-processing relies on simplified prescriptions for photon escape, and the calculations are local rather than global. Future

simulations including radiation coupling, global disk structure, and orbital evolution will be necessary to refine these predictions.

Despite these limitations, the present work shows that black hole–disk collisions can naturally produce long-lived, soft-X-ray accretion-powered flares. More complete radiation-hydrodynamics computations and future observations of repeating nuclear transients will be essential for testing the relevance of this scenario to QPE-like sources and related systems.

ACKNOWLEDGEMENTS

The authors thank Pietro Baldini, Kenta Hotokezaka, Christopher Irwin, Itai Linial, Tatsuya Matsumoto, and Andrew Mummery for useful discussions. This work benefited from discussions during the Yukawa Institute for Theoretical Physics (YITP) workshop YITP-T-25-02, “Multi-Messenger Astrophysics in the Dynamic Universe”. The authors thank the YITP at Kyoto University for hospitality during the workshop. Numerical computations were performed on the Sakura cluster at the Max Planck Computing and Data Facility (MPCDF). This work was in part supported by Grant-in-Aid for Scientific Research (grant No. 23H04900) of Japanese MEXT/JSPS. A.T.L.L. acknowledges support by NASA under award No. 80NSSC25K7213.

SOFTWARE

This work made use of the Julia programming language (Bezanson et al. 2017) and the following packages: Makie.jl (Danisch & Krumbiegel 2021) for visualization, DataFrames.jl (Bouchet-Valat & Kamiński 2023) for data handling, and Eikonal.jl for solving the eikonal equation for the optical depth.

DATA AVAILABILITY

The data underlying this article will be shared on reasonable request to the corresponding author.

REFERENCES

Alexander T., 2005, *Physics Reports*, 419, 65
 Amaro-Seoane P., 2018, *Living Reviews in Relativity*, 21, 4
 Amaro-Seoane P., Gair J. R., Freitag M., Coleman Miller M., Mandel L., Cutler C. J., Babak S., 2007, *Class. Quant. Grav.*, 24, R113
 Amaro-Seoane P., et al., 2017, arXiv preprint arXiv:1702.00786
 Amati L., O’Brien P. T., Götz D., Bozzo E., Santangelo A., 2021, in *Space Telescopes and Instrumentation 2020: Ultraviolet to Gamma Ray*. pp 395–406
 Antonini F., 2014, *The Astrophysical Journal*, 794, 106
 Antonini F., Perets H. B., 2012, *The Astrophysical Journal*, 757, 27
 Arcodia R., et al., 2021, *Nature*, 592, 704
 Arcodia R., et al., 2022, *Astronomy & Astrophysics*, 662, A49
 Arcodia R., et al., 2024a, *Astronomy & Astrophysics*, 684, A64
 Arcodia R., et al., 2024b, *Astronomy & Astrophysics*, 684, L14
 Arcodia R., et al., 2025, *The Astrophysical Journal*, 989, 13
 Babak S., et al., 2017, *Physical Review D*, 95, 103012
 Bahcall J. N., Wolf R. A., 1976, *Astrophysical Journal*, vol. 209, Oct. 1, 1976, pt. 1, p. 214–232., 209, 214
 Bahcall J. N., Wolf R., 1977, *Astrophysical Journal*, Part 1, vol. 216, Sept. 15, 1977, p. 883–907., 216, 883
 Baldini P., et al., 2026, arXiv preprint arXiv:2602.03932
 Barcons X., et al., 2017, *Astronomische Nachrichten*, 338, 153

Bartos I., Kocsis B., Haiman Z., Márka S., 2017, *The Astrophysical Journal*, 835, 165
 Bezanson J., Edelman A., Karpinski S., Shah V. B., 2017, *SIAM review*, 59, 65
 Bondi H., Hoyle F., 1944, *Monthly Notices of the Royal Astronomical Society*, 104, 273
 Bouchet-Valat M., Kamiński B., 2023, *Journal of Statistical Software*, 107, 1
 Bykov S., Gilfanov M., Sunyaev R., Medvedev P., 2025, *Monthly Notices of the Royal Astronomical Society*, 540, 30
 Chakraborty J., Kara E., Masterson M., Giustini M., Miniutti G., Saxton R., 2021, *The Astrophysical Journal Letters*, 921, L40
 Chakraborty J., et al., 2024, *The Astrophysical Journal*, 965, 12
 Chakraborty J., et al., 2025a, *The Astrophysical Journal Letters*, 983, L39
 Chakraborty J., et al., 2025b, *The Astrophysical Journal*, 984, 124
 Chakraborty J., et al., 2025c, *The Astrophysical Journal*, 992, 120
 Chakraborty J., et al., 2026, arXiv preprint arXiv:2602.16776
 Chen X., Qiu Y., Li S., Liu F., 2022, *The Astrophysical Journal*, 930, 122
 Chitan A., Gallagher S. C., Abbassi S., 2026, *The Astrophysical Journal*, 998, 322
 Dai L., Fuerst S. V., Blandford R., 2010, *Monthly Notices of the Royal Astronomical Society*, 402, 1614
 Dai J. L., Lodato G., Cheng R., 2021, *Space Science Reviews*, 217, 12
 Danisch S., Krumbiegel J., 2021, *Journal of Open Source Software*, 6, 3349
 Dodd S. A., Huang X., Davis S. W., Ramirez-Ruiz E., 2025, arXiv preprint arXiv:2506.19900
 Duque F., Kejriwal S., Sberna L., Speri L., Gair J., 2025, *Physical Review D*, 111, 084006
 Edgar R., 2004, *New Astronomy Reviews*, 48, 843
 Franchini A., et al., 2023, *Astronomy & Astrophysics*, 675, A100
 Frank J., King A., Raine D. J., 2002, *Accretion Power in Astrophysics: Third Edition*
 Gezari S., 2021, *Annual Review of Astronomy and Astrophysics*, 59, 21
 Giustini M., Miniutti G., Saxton R. D., 2020, *Astronomy & Astrophysics*, 636, L2
 Goodman J., Tan J. C., 2004, *The Astrophysical Journal*, 608, 108
 Goodwin A., et al., 2024, *Monthly Notices of the Royal Astronomical Society*, 528, 7123
 Guo W., Shen R.-F., 2026, *The Astrophysical Journal*, 998, 78
 Guo H., et al., 2026, arXiv preprint arXiv:2603.02517
 Hernández-García L., et al., 2025a, *Nature Astronomy*, 9, 895
 Hernández-García L., et al., 2025b, *Astronomy & Astrophysics*, 703, A263
 Homan D., et al., 2023, *Astronomy & Astrophysics*, 672, A167
 Hopman C., Alexander T., 2006, *The Astrophysical Journal Letters*, 645, L133
 Hoyle F., Lyttleton R. A., 1939, in *Mathematical proceedings of the Cambridge philosophical society*. pp 405–415
 Huang X., Linial I., Jiang Y.-F., 2025, *The Astrophysical Journal*, 993, 186
 Huang S., Huang X., Zhu Z., Martin R. G., 2026, *Resolving Oblique Star-Disk Collisions in Quasi-Periodic Eruptions: Numerical Requirements and the Importance of Geometry* (arXiv:2604.00953), <https://arxiv.org/abs/2604.00953>
 Inayoshi K., Haiman Z., Ostriker J. P., 2016, *Monthly Notices of the Royal Astronomical Society*, 459, 3738
 Ingram A., Motta S. E., Aigrain S., Karastergiou A., 2021, *Monthly Notices of the Royal Astronomical Society*, 503, 1703
 Ivanov P. B., Igumenshchev I. V., Novikov I. D., 1998, *The Astrophysical Journal*, 507, 131
 Jankovič T., Bonnerot C., Karpov S., Jurca A., 2026, arXiv preprint arXiv:2602.02656
 Jansen F., et al., 2001, *Astronomy & Astrophysics*, 365, L1
 Jiang N., Pan Z., 2025, *The Astrophysical Journal Letters*, 983, L18
 Jiang Y.-F., Stone J. M., Davis S. W., 2014, *The Astrophysical Journal*, 796, 106
 Jiang H.-X., Li X., Mizuno Y., Younsi Z., Fromm C. M., 2026, arXiv preprint arXiv:2603.10792
 Katz B., Budnik R., Waxman E., 2010, *The Astrophysical Journal*, 716, 781
 Kaur K., Stone N. C., Gilbaum S., 2023, *Monthly Notices of the Royal Astronomical Society*, 524, 1269

- Kejriwal S., Witzany V., Zajaček M., Pasham D. R., Chua A. J., 2024, *Monthly Notices of the Royal Astronomical Society*, 532, 2143
- King A., 2022, *Monthly Notices of the Royal Astronomical Society*, 515, 4344
- Kitaki T., Mineshige S., Ohsuga K., Kawashima T., 2018, *Publications of the Astronomical Society of Japan*, 70, 108
- Kitaki T., Mineshige S., Ohsuga K., Kawashima T., 2021, *Publications of the Astronomical Society of Japan*, 73, 450
- Kocsis B., Yunes N., Loeb A., 2011, *Physical Review D—Particles, Fields, Gravitation, and Cosmology*, 84, 024032
- Komossa S., et al., 2023, *Monthly Notices of the Royal Astronomical Society: Letters*, 522, L84
- Krolik J. H., Liniel I., 2022, *The Astrophysical Journal*, 941, 24
- Lam A. T.-L., Shibata M., 2025, *Physical Review D*, 111, 103039
- Lam A. T.-L., Shibata M., Kawaguchi K., Pelle J., 2025, *Physical Review D*, 112, 083006
- Lehto H. J., Valtonen M. J., 1996, *Astrophysical Journal* v. 460, p. 207, 460, 207
- Levin Y., 2007, *Monthly Notices of the Royal Astronomical Society*, 374, 515
- Liniel I., Metzger B. D., 2023, *The Astrophysical Journal*, 957, 34
- Liniel I., Metzger B. D., 2024, *The Astrophysical Journal Letters*, 963, L1
- Liniel I., Metzger B. D., Quataert E., 2025, *The Astrophysical Journal*, 991, 147
- Liu K., Liu S.-F., Pan Z., Deng H., Shen R., Yu C., 2026, arXiv preprint arXiv:2603.00226
- Lui L., Torres-Orjuela A., Chowdhury R. K., Dai L., 2025, arXiv preprint arXiv:2508.07961
- Luo J., et al., 2016, *Classical and Quantum Gravity*, 33, 035010
- McKernan B., Ford K., Lyra W., Perets H., 2012, *Monthly Notices of the Royal Astronomical Society*, 425, 460
- McKernan B., Ford K., Kocsis B., Lyra W., Winter L., 2014, *Monthly Notices of the Royal Astronomical Society*, 441, 900
- Metzger B. D., Stone N. C., Gilbaum S., 2022, *The Astrophysical Journal*, 926, 101
- Middleton M., et al., 2025, *Monthly Notices of the Royal Astronomical Society*, 537, 1688
- Miniutti G., et al., 2019, *Nature*, 573, 381
- Mummery A., 2025, *Monthly Notices of the Royal Astronomical Society*, p. staf1658
- Mummery A., Balbus S. A., 2020, *Monthly Notices of the Royal Astronomical Society*, 492, 5655
- Nakar E., Sari R., 2010, *The Astrophysical Journal*, 725, 904
- Netzer H., 2015, *Annual Review of Astronomy and Astrophysics*, 53, 365
- Nicholl M., et al., 2024, *Nature*, 634, 804
- Novikov I. D., Thorne K. S., 1973, in Dewitt C., Dewitt B. S., eds, *Black Holes (Les Astres Occlus)*. pp 343–450
- O’Leary R. M., Kocsis B., Loeb A., 2009, *Monthly Notices of the Royal Astronomical Society*, 395, 2127
- Ohsuga K., Mineshige S., 2011, *The Astrophysical Journal*, 736, 2
- Pan X., Li S.-L., Cao X., Miniutti G., Gu M., 2022, *The Astrophysical Journal Letters*, 928, L18
- Pasham D. R., et al., 2024, *Science Advances*, 10, eadj8898
- Perego A., Rosswog S., Cabezón R. M., Korobkin O., Käppeli R., Arcones A., Liebendörfer M., 2014, *Monthly Notices of the Royal Astronomical Society*, 443, 3134
- Pihajoki P., 2016, *Monthly Notices of the Royal Astronomical Society*, 457, 1145
- Piran T., Svirski G., Krolik J., Cheng R. M., Shiokawa H., 2015, *The Astrophysical Journal*, 806, 164
- Quintin E., et al., 2023, *Astronomy & Astrophysics*, 675, A152
- Raj A., Nixon C., 2021, *The Astrophysical Journal*, 909, 82
- Rees M. J., 1988, *Nature*, 333, 523
- Ressler S. M., Combi L., Li X., Ripperda B., Yang H., 2024, *The Astrophysical Journal*, 967, 70
- Ressler S. M., Combi L., Ripperda B., Li X., 2025, *The Astrophysical Journal Letters*, 993, L22
- Rose S. C., Naoz S., Sari R., Liniel I., 2022, *The Astrophysical Journal Letters*, 929, L22
- Sadowski A., Wielgus M., Narayan R., Abarca D., McKinney J. C., Chael A., 2017, *Monthly Notices of the Royal Astronomical Society*, 466, 705
- Sánchez-Sáez P., et al., 2024, *Astronomy & Astrophysics*, 688, A157
- Shakura N. I., Sunyaev R. A., 1973, *Astronomy and Astrophysics*, Vol. 24, p. 337-355, 24, 337
- Sillanpaa A., Haarala S., Valtonen M., Sundelius B., Byrd G., 1988, *Astrophysical Journal*, Part 1 (ISSN 0004-637X), vol. 325, Feb. 15, 1988, p. 628-634. Research supported by Nordisk Institut for Teoretisk Atomfysik and NSF., 325, 628
- Sniegowska M., Czerny B., Bon E., Bon N., 2020, *Astronomy & Astrophysics*, 641, A167
- Speri L., Antonelli A., Sberna L., Babak S., Barausse E., Gair J. R., Katz M. L., 2023, *Physical Review X*, 13, 021035
- Stone N. C., Metzger B. D., Haiman Z., 2017, *Monthly Notices of the Royal Astronomical Society*, 464, 946
- Suková P., Zajaček M., Witzany V., Karas V., 2021, *The Astrophysical Journal*, 917, 43
- Suzuguchi T., Matsumoto T., 2026, *Monthly Notices of the Royal Astronomical Society*, 545, staf2243
- Suzuguchi T., Omiya H., Takeda H., 2026, *Publications of the Astronomical Society of Japan*, 78, 185
- Tagawa H., Haiman Z., 2023, *Monthly Notices of the Royal Astronomical Society*, 526, 69
- Tagawa H., Haiman Z., Kocsis B., 2020, *The Astrophysical Journal*, 898, 25
- Toyouchi D., Hotokezaka K., Inayoshi K., Kuiper R., 2024, *Monthly Notices of the Royal Astronomical Society*, 532, 4826
- Urry C. M., Padovani P., 1995, *Publications of the Astronomical Society of the Pacific*, 107, 803
- Valtonen M. J., et al., 2008, *Nature*, 452, 851
- Valtonen M. J., et al., 2023, *Monthly Notices of the Royal Astronomical Society*, 525, 1153
- Vurm I., Liniel I., Metzger B. D., 2025, *The Astrophysical Journal*, 983, 40
- Weaver T. A., 1976, *Astrophysical Journal Supplement Series*, vol. 32, Oct. 1976, p. 233-282., 32, 233
- Wevers T., Pasham D., Jalan P., Rakshit S., Arcodia R., 2022, *Astronomy & Astrophysics*, 659, L2
- Xian J., Zhang F., Dou L., He J., Shu X., 2021, *The Astrophysical Journal Letters*, 921, L32
- Yang Y., et al., 2019, *Physical Review Letters*, 123, 181101
- Yao P. Z., Quataert E., Jiang Y.-F., Lu W., White C. J., 2025, *The Astrophysical Journal*, 978, 91
- Yuan W., Zhang C., Chen Y., Ling Z., 2022, in , *Handbook of X-ray and Gamma-ray Astrophysics*. Springer, pp 1–30
- Zhan Y., Zhang D., Yi S.-X., Wang F.-Y., 2026, *The Astrophysical Journal*, 997, 134
- Zhao H., 2005, *Mathematics of computation*, 74, 603
- Zhao Z., Wang Y., Zou Y., Wang F., Dai Z., 2022, *Astronomy & Astrophysics*, 661, A55
- Zhou C., Huang L., Guo K., Li Y.-P., Pan Z., 2024a, *Physical Review D*, 109, 103031
- Zhou C., Zhong B., Zeng Y., Huang L., Pan Z., 2024b, *Physical Review D*, 110, 083019
- Zhu J., et al., 2025, *The Astrophysical Journal Letters*, 994, L16

APPENDIX A: SHOCK IDENTIFICATION

We identify shocks at cell interfaces by comparing primitive variables on the left (L) and right (R) sides of each interface. Let v_n denote the velocity component normal to the interface, ρ the mass density, p the gas pressure, and $s = p/\rho^\Gamma$ an entropy measure, with Γ the adiabatic index. We classify the upstream state by requiring that the normal

velocity decreases across the interface from left to right⁶ and that density, pressure, and entropy increase in the downstream direction. Specifically, the left state is identified as upstream if

$$\begin{aligned} \rho_L < \rho_R, \quad v_{n,L} > v_{n,R}, \\ p_L < p_R, \quad s_L < s_R, \end{aligned} \quad (\text{A1})$$

while the right state is identified as upstream if

$$\begin{aligned} \rho_L > \rho_R, \quad v_{n,L} > v_{n,R}, \\ p_L > p_R, \quad s_L > s_R. \end{aligned} \quad (\text{A2})$$

Interfaces that satisfy neither set of inequalities are not classified as shocks. At cell interfaces where shocks are detected, the shock speed is estimated using the Rankine–Hugoniot relations. Namely,

$$v_{\text{sh}} = v_u \pm c_{s,u} \sqrt{1 + \frac{\Gamma + 1}{2\Gamma} \left(\frac{p_d}{p_u} - 1 \right)}, \quad (\text{A3})$$

with $c_s = \sqrt{\Gamma p / \rho}$ the sound speed. The sign is chosen so that the upstream velocity in the shock frame, $v_u - v_{\text{sh}}$, points towards the interface (i.e. the plus sign when the upstream is the left state, and the minus sign when the upstream is the right state).

APPENDIX B: ADVECTION TRAPPING FACTOR

Our advection-trapping factor is motivated by a steady toy model constructed on top of a given hydrodynamic profile, (ρ_0, \vec{v}_0, e_0) , where $e_0 = \rho_0 \varepsilon_0$ is the internal energy density. Assuming a quasi-steady state and radiation-dominated internal energy ($\Gamma = 4/3$), the underlying hydrodynamic profile satisfies

$$\nabla \cdot \left[\left(\frac{1}{2} \rho_0 v_0^2 + \frac{4}{3} e_0 \right) \vec{v}_0 \right] = 0. \quad (\text{B1})$$

If we considered the photon diffusion flux, the result would be a different profile (ρ, \vec{v}, e) satisfying

$$\nabla \cdot \left[\left(\frac{1}{2} \rho v^2 + \frac{4}{3} e \right) \vec{v} - \frac{c}{3\kappa\rho} \nabla e \right] = 0. \quad (\text{B2})$$

Approximating $(\rho, \vec{v}) \approx (\rho_0, \vec{v}_0)$ and using Eq. (B1), then

$$\nabla \cdot \left[\left(\frac{4}{3} (e - e_0) \right) \vec{v} - \frac{c}{3\kappa\rho} \nabla e \right] = 0, \quad (\text{B3})$$

In a one-dimensional problem, the equation becomes

$$\frac{de}{d\tau} + \frac{4v}{c} (e - e_0) = \text{const.}, \quad (\text{B4})$$

which yields exponential attenuation with depth in the presence of inward flow ($v < 0$). Therefore, we define the advection trapping factor along an escape path γ_{esc} as:

$$f_{\text{adv}} := \exp \left[-\frac{4}{c} \int_{\gamma_{\text{esc}}} v^- d\tau \right], \quad v^- := \min(v_r, 0), \quad (\text{B5})$$

where v_r is the radial velocity component and $d\tau = \kappa\rho dl$ is the differential optical depth along γ_{esc} .

This paper has been typeset from a $\text{\TeX}/\text{\LaTeX}$ file prepared by the author.

⁶ This condition holds regardless of the orientation of the shock: if the right state is upstream, $v_{n,R} < v_{n,L} < 0$; if the left state is upstream, $0 < v_{n,R} < v_{n,L}$.